Rotated versions of the Jablonowski steady-state and baroclinic wave test cases: A dynamical core intercomparison

Peter H. Lauritzen [1]*, Christiane Jablonowski* [2]*, Mark A. Taylor* [3]*, and Ramachandran D. Nair* [4]

[1]Climate and Global Dynamics, National Center for Atmospheric Research, Boulder, CO, USA.
[2]University of Michigan, Department of Atmospheric, Oceanic and Space Sciences, Ann Arbor, MI, USA.
[3]Sandia National Laboratories, Albuquerque, New Mexico, USA.
[4]Institute for Mathematics Applied to Geosciences, National Center for Atmospheric Research, Boulder, CO, USA.

The Jablonowski test case is widely used for debugging and evaluating the numerical characteristics of global dynamical cores that describe the fluid dynamics component of Atmospheric General Circulation Models. The test is defined in terms of a steady-state solution to the equations of motion and an overlaid perturbation that triggers a baroclinically unstable wave. The steady-state initial conditions are zonally symmetric. Therefore, the test case design has the potential to favor models that are built upon regular latitude-longitude or Gaussian grids. Here we suggest rotating the computational grid so that the balanced flow is no longer aligned with the computational grid latitudes. Ideally the simulations should be invariant under rotation of the computational grid. Note that the test case only requires an adjustment of the Coriolis parameter in the model code.

The rotated test case has been exercised by six dynamical cores. In addition, two of the models have been tested with different vertical coordinates resulting in a total of eight model variants. The models are built with different computational grids (regular latitude-longitude, cubed-sphere, icosahedral hexagonal/triangular) and use very different numerical schemes. The test-case is a useful tool for debugging, assessing the degree of anisotropy in the numerical methods and grids, and evaluating the numerical treatment of the pole points since the rotated test case directs the flow directly over the geographical poles. Special treatments such as polar filters are therefore more exposed in this rotated test case.

1. Introduction

The need for developing global test cases for dynamical cores is becoming increasingly important as modeling groups move towards seamless modeling systems where the same flow solvers are intended for both high *weather* resolutions as well as for coarser *climate* resolutions. Hence the dynamical core should be accurate across an even wider range of scales. To meet the requirements of a high degree of computational parallelism and scalability in the numerical algorithms non-traditional spherical grids, that are more isotropic than the widely used regular latitude-longitude grids, are being explored. In addition, novel numerical techniques are being assessed by the global atmospheric modeling community. All these factors raise questions about the accuracy of these new models as compared to traditional approaches that have been tested and used extensively during the last 20-30 years.

At any resolution it is inevitable that a numerical method introduces errors and thereby misrepresent the flow in some way. It is hard to distinguish cause and effect in model runs with parameterized physical processes. Therefore, running idealized test cases have become standard during model development. Standard test cases for passive tracer transport (see Machenhauer et al. 2008 for an overview) and two-dimensional shallow water tests (e.g., Williamson et al. 1992, Galewsky et al. 2004, Läuter et al. 2005) are well estab-

To whom correspondence should be addressed.
Peter Hjort Lauritzen, Climate and Global Dynamics, National Center for Atmospheric Research, 1850 Table Mesa Drive, Boulder, CO, 80305, USA.
e-mail: pel@ucar.edu

lished in the atmospheric modeling community whereas global test cases for three dimensional models are not as widespread. A global test case gaining popularity was recently proposed by Jablonowski (2004) and examined by Jablonowski and Williamson (2006a; hereafter referred to as JW06). It consists of a steady-state solution and a baroclinic wave resulting from adding a perturbation to the steady-state initial condition. The Jablonowski test case targets the large scale (hydrostatic) performance of the model and its ability to retain a balanced flow. An analytic solution exists for the steady-state test case provided the model utilizes a hydrostatic or non-hydrostatic shallow-atmosphere equation set. No analytic solution exists for the baroclinic wave test and therefore the 'exact' solution must be approximated numerically. The test is deterministic and convergence can be established based on an ensemble of high resolution reference solutions (JW06). Other idealized test cases for three-dimensional dynamical cores have also recently been proposed by Polvani et al. (2004), Staniforth and White (2008b), Staniforth and White (2008c) and Jablonowski et al. (2009). In addition, test cases targeting the smaller scale and non-hydrostatic performance of the dynamical cores were suggested by Wedi and Smolarkiewicz (2009). Global non-hydrostatic models should also be able to retain large scale balances in the flow. It is therefore expected that the non-hydrostatic models run at hydrostatic resolutions (scales) converge to the hydrostatic model reference solutions.

Here we propose a variant of the Jablonowski test cases where the physical flow remains the same but the computational grid is rotated with respect to the physical flow. Ideally the dynamical core should be invariant under rotation of the computational grid. However, usually the numerical algorithms are less challenged when the flow is aligned or quasi-aligned with the computational grid in contrast to flows that predominantly traverse the computational grid lines at a slantwise angle. Therefore the Jablonowski test cases somewhat favors regular latitude-longitude grids since the flow is predominantly parallel to the latitude circles throughout the domain. The grid rotations suggested in this paper are schematically explained in Fig. 1. The figure shows a regular latitude-longitude grid with different rotation angles α that are superimposed upon a zonally symmetric flow field. The white thick lines depict the rotated coordinate system in geographical coordinates. In the rotated latitude-longitude grids the flow is no longer aligned with the coordinate lines throughout the global domain of integration, thereby challenging the schemes' ability to maintain balances in the flow.

In this paper we present results from six dynamical cores that participated in a 2-week summer colloquium at the National Center for Atmospheric Research (NCAR) in 2008 [1]. In addition, two of the models are tested with different vertical coordinates resulting in a total of eight model variants. The colloquium was entitled *Numerical Techniques for Global Atmospheric Models* and was part of the annual NCAR Advanced Study Program (ASP) colloquium series (for more information see http://www.cgd.ucar.edu/cms/pel/colloquium.html). Apart from its educational aspects the summer colloquium presented an unprecedented opportunity to intercompare a wide range of global dynamical cores with different spherical grids and numerical methods. All models were tested with an identical dynamical core test suite that is documented in Jablonowski et al. (2009).

The paper is organized as follows. In Section 2 the rotated test case is defined. In Section 3 we briefly describe the suite of models that ran the test cases. Section 4 discusses the simulation results followed by conclusions in Section 5.

2. Test case description

Since the new rotated test case is expressed in terms of the unrotated test case described in JW06, we first present the unrotated initial conditions. Then the rotated initial conditions are formulated.

2.1. Unrotated initial conditions

2.1.1. Steady-state

The initial conditions comprise a zonally symmetric basic state with a jet in the midlatitudes of each hemisphere and a quasi-realistic temperature distribution. They are formulated in terms of the zonal wind component u, meridional wind component v, temperature T, surface pressure p_s and surface geopotential Φ_s. Extensions to other prognostic variable sets are straightforward. In addition, we assume vertical coordinates that are typically used in General Circulation Models (GCMs) today. These are the pressure-based $\sigma = p/p_s$ (Phillips 1957) coordinate or an η (hybrid $\sigma - p$; Simmons and Burridge

---

[1]results from participating models that did not produce a complete dataset are not included in this study
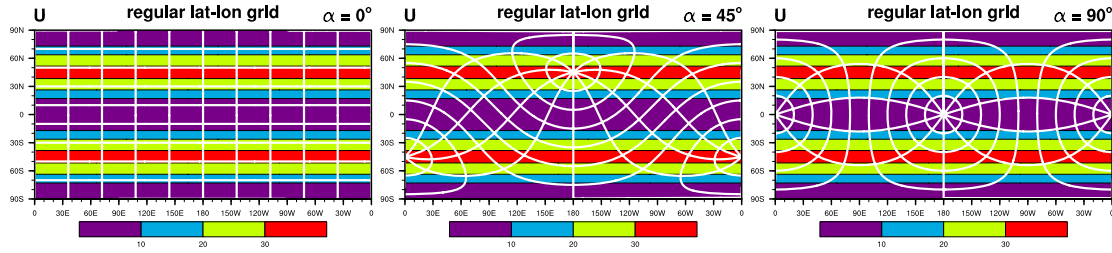
Figure 1: Color scales show the zonal wind (m s^{-1}) at model level 3 near 14 hPa. White solid lines show the regular latitude-longitude grid rotated at the angle $\alpha = 0°$ (left), $\alpha = 45°$ (middle) and $\alpha = 90°$ (right), respectively. The coordinate axis refer to the geographical coordinates.

k	$A_{k+\frac{1}{2}}$	$B_{k+\frac{1}{2}}$	k	$A_{k+\frac{1}{2}}$	$B_{k+\frac{1}{2}}$	k	$A_{k+\frac{1}{2}}$	$B_{k+\frac{1}{2}}$
0	0.002194067	0.	9	0.07590131	0.03276228	18	0.04468960	0.4243822
1	0.004895209	0.	10	0.07424086	0.05359622	19	0.03752191	0.5143168
2	0.009882418	0.	11	0.07228744	0.07810627	20	0.02908949	0.6201202
3	0.01805201	0.	12	0.06998933	0.1069411	21	0.02084739	0.7235355
4	0.02983724	0.	13	0.06728574	0.1408637	22	0.01334443	0.8176768
5	0.04462334	0.	14	0.06410509	0.1807720	23	0.00708499	0.8962153
6	0.06160587	0.	15	0.06036322	0.2277220	24	0.00252136	0.9534761
7	0.07851243	0.	16	0.05596111	0.2829562	25	0.	0.9851122
8	0.07731271	0.01505309	17	0.05078225	0.3479364	26	0.	1.

Table 1: Vertical coefficients used do define the hybrid η-vertical coordinate, where k is the vertical index, the parameter $A_{k+\frac{1}{2}}$ denotes the pure pressure component and $B_{k+\frac{1}{2}}$ defines the σ part of the vertical coordinate. The coefficients are the same as used in JW06.

1981) vertical coordinate as defined by

$$p(\lambda, \varphi, \eta) = A(\eta)p_0 + B(\eta)p_s(\lambda, \varphi) . \qquad (2.1)$$

The interface coefficients A and B (half indices) are given in Table 1, $\lambda \in [0, 2\pi]$ and $\varphi \in [-\pi/2, \pi/2]$ denote the longitudinal and latitudinal directions, the reference pressure p_0 is set to 1000 hPa, and the initial surface pressure p_s is constant and set to $p_s = 1000$ hPa. Throughout this paper, 26 vertical model levels are used. The hybrid coordinate $\eta \in [0, 1]$ is unity at the surface and approaches a constant at the model top. Note that the value of p_0 might not be standard in all GCMs that utilize the hybrid vertical coordinate system.

The flow field is comprised of two symmetric non-divergent zonal jets in the midlatitudes:

$$u_{steady}(\lambda, \varphi, \eta) = u_0 \cos^{\frac{3}{2}} \eta_v \sin^2 (2\varphi) \quad (2.2)$$
$$v_{steady}(\lambda, \varphi, \eta) = 0 \qquad\qquad (2.3)$$

where η_v is defined as $\eta_v = 0.5(\eta - \eta_0)\pi$, $\eta_0 = 0.252$

is the center position of the jet, and the maximum amplitude u_0 is set to 35 m s^{-1}. This velocity distribution resembles the zonal-mean time-mean jet streams in the troposphere. For non-hydrostatic models the vertical velocity is set to zero.

The temperature distribution consists of a horizontal-mean temperature and a horizontal variation at each level. The horizontally averaged temperature $\bar{T}(\eta)$ is given by

$$\bar{T}(\eta) = \begin{cases} T_0 \, \eta^{\frac{R_d \Gamma}{g}} & \text{for } \eta_s \geq \eta \geq \eta_t \\ T_0 \, \eta^{\frac{R_d \Gamma}{g}} + \Delta T \, (\eta_t - \eta)^5 & \text{for } \eta_t > \eta \end{cases}$$
$$(2.4)$$

with the surface level $\eta_s = 1$, tropopause level $\eta_t = 0.2$ and horizontal-mean temperature at the surface $T_0 = 288$ K. The temperature lapse rate Γ is set to 0.005 K m^{-1} which is similar to the observed diabatic lapse rate. The empirical temperature difference ΔT is set to 4.8×10^5 K, $R_d = 287.04$ J (kg K)$^{-1}$ represents the ideal gas constant for dry air and $g = 9.80616$ m s^{-2}

is the gravitational acceleration. The three-dimensional temperature distribution is then defined by

$$T(\lambda, \varphi, \eta) = \bar{T}(\eta) + \frac{3}{4} \frac{\eta \pi u_0}{R_d} \sin \eta_v \, \cos^{\frac{1}{2}} \eta_v \, \times$$
$$\left\{ \left(- 2 \sin^6 \varphi \, (\cos^2 \varphi + \frac{1}{3}) + \frac{10}{63} \right) \times \right.$$
$$2 \, u_0 \cos^{\frac{3}{2}} \eta_v +$$
$$\left. \left(\frac{8}{5} \cos^3 \varphi \, (\sin^2 \varphi + \frac{2}{3}) - \frac{\pi}{4} \right) a \, \Omega \right\}, \tag{2.5}$$

where $\Omega = 7.29212 \times 10^{-5}$ s^{-1} is the Earth's angular velocity and $a = 6.371229 \times 10^6$ m is the radius of the Earth. The geopotential $\Phi = gz$ completes the description of the steady-state initial conditions where z symbolizes the elevation of a model level η. The total geopotential distribution comprises the horizontal-mean geopotential $\bar{\Phi}$ and a horizontal variation at each level. This is analogous to the description of the temperature field. The geopotential is given by

$$\Phi(\lambda, \varphi, \eta) = \bar{\Phi}(\eta) + u_0 \, cos^{\frac{3}{2}} \eta_v \, \times$$
$$\left\{ \left(- 2 \sin^6 \varphi \, (\cos^2 \varphi + \frac{1}{3}) + \frac{10}{63} \right) \times \right.$$
$$u_0 \cos^{\frac{3}{2}} \eta_v +$$
$$\left. \left(\frac{8}{5} \cos^3 \varphi \, (\sin^2 \varphi + \frac{2}{3}) - \frac{\pi}{4} \right) a \, \Omega \right\}, \tag{2.6}$$

with

$$\bar{\Phi}(\eta) = \begin{cases} \frac{T_0 \, g}{\Gamma} \left(1 - \eta^{\frac{R_d \Gamma}{g}} \right) & \text{for } \eta_s \geq \eta \geq \eta_t \\ \frac{T_0 \, g}{\Gamma} \left(1 - \eta^{\frac{R_d \Gamma}{g}} \right) - \mathcal{K} & \text{for } \eta_t > \eta \end{cases} \tag{2.7}$$

where

$$\mathcal{K} = R_d \, \Delta T \, \times \left\{ \left(\ln \left(\frac{\eta}{\eta_t} \right) + \frac{137}{60} \right) \eta_t^5 \right.$$
$$\left. - 5 \, \eta_t^4 \, \eta + 5 \, \eta_t^3 \, \eta^2 - \frac{10}{3} \, \eta_t^2 \, \eta^3 + \frac{5}{4} \, \eta_t \, \eta^4 - \frac{1}{5} \, \eta^5 \right\}. \tag{2.8}$$

This formulation enforces the hydrostatic balance analytically and ensures the continuity of the geopotential at the tropopause level η_t. In hydrostatic models with pressure-based vertical coordinates, it is only necessary to initialize the surface geopotential $\Phi_s = gz_s$. It balances the non-zero zonal wind at the surface with surface elevation z_s and is determined by setting $\eta = \eta_s$ in

(2.6). This leads to the following equation for the surface geopotential

$$\Phi_s(\lambda, \varphi) = u_0 \, \cos^{\frac{3}{2}} \left((\eta_s - \eta_0) \frac{\pi}{2} \right) \times$$
$$\left\{ \left(- 2 \sin^6 \varphi \, (\cos^2 \varphi + \frac{1}{3}) + \frac{10}{63} \right) \times \right.$$
$$u_0 \cos^{\frac{3}{2}} \left((\eta_s - \eta_0) \frac{\pi}{2} \right) +$$
$$\left. \left(\frac{8}{5} \cos^3 \varphi \, (\sin^2 \varphi + \frac{2}{3}) - \frac{\pi}{4} \right) a \, \Omega \right\}. \tag{2.9}$$

Note that Φ_s is a function of latitude only. The geopotential equation (2.6) can fully be utilized for dynamical cores with height-based vertical coordinates. Then, a root-finding algorithm is recommended to determine the corresponding η-level for any given height z. This iterative method, which is also applicable to isentropic vertical coordinates, is outlined in the Appendix of JW06. The resulting η-level is accurate to machine precision and can consequently be used to compute the initial data set.

The test design guarantees static, inertial and symmetric stability properties, but is unstable with respect to baroclinic or barotropic instability mechanisms.

2.1.2. Baroclinic wave

A baroclinic wave can be triggered if the initial conditions for the steady-state test described in the previous subsection are overlaid with a perturbation. Here a perturbation with a Gaussian profile is selected and centered at $(\lambda_c, \varphi_c) = (\pi/9, 2\pi/9)$ which points to the location (20°E,40°N). The perturbation overlays the zonal wind field. The zonal wind perturbation u_{pert} is given by

$$u_{pert}(\lambda, \varphi, \eta) = u_p \, \exp \left(- \left(\frac{r}{R} \right)^2 \right) \tag{2.10}$$

with the great circle distance r

$$r = a \, \arccos \left(\sin \varphi_c \, \sin \varphi + \cos \varphi_c \, \cos \varphi \, \cos(\lambda - \lambda_c) \right) . \tag{2.11}$$

The radius of the perturbation is $R = a/10$. The maximum perturbation amplitude is set to $u_p = 1$ m s^{-1}. It is superimposed on the balanced zonal wind field (2.2) by adding u_{pert} to the wind field at each grid point at all model levels:

$$u_{wave}(\lambda, \varphi, \eta) = u_{steady} + u_{pert} \tag{2.12}$$

The meridional wind component is zero as in the steady-state initial condition: $v_{wave} = v_{steady} = 0$.

The baroclinic wave, although idealized, represents very realistic flow features. Strong temperature fronts develop that are associated with the evolving low and high pressure systems. Note that the baroclinic wave test case does not have an analytic solution. Therefore, high resolution reference solutions and their uncertainties are used (JW06).

2.2. Rotated initial conditions

The rotated initial conditions are formulated in terms of the unrotated initial conditions. The physical flow remains the same but the computational grid is rotated with respect to the physical flow. However, two changes are necessary. First, because of the rotations the Coriolis parameter f is a function of both latitude φ and longitude θ:

$$f(\lambda, \varphi) = 2\Omega \left(- \cos \lambda \cos \varphi \sin \alpha + \sin \varphi \cos \alpha \right). \tag{2.13}$$

Second, the initial conditions need to be rotated. The rotation is schematically depicted in Fig. 2 that shows the location of the rotated North pole (λ_p, φ_p) with respect to the North (N) and South (S) poles of the unrotated Earth. In short, the rotated coordinate locations (λ', φ') need to be determined in terms of the unrotated coordinates (λ, φ). This allows the analytical evaluation of the initial conditions at that location. Note that the unrotated coordinates are also referred to as the geographical coordinates.

2.2.1. Transformations for rotated coordinates

The rotation of the coordinates, together with their inverse relations, has been described in, e.g., Ritchie (1987), Nair and Jablonowski (2008) and Staniforth and White (2008a). Note that the trigonometric functions as outlined below might suffer from precision problems due to multiple applications of trigonometric functions. Therefore, a slightly different but highly precise method has been implemented in the Fortran example code made available to the modeling groups on the NCAR web page http://www.cgd.ucar.edu/cms/pel/colloquium_links.html.

The following steps illustrate the basic principle behind the rotations. Let the North pole of a rotated coordinate system (λ', θ') be located at the point (λ_p, φ_p) of the regular unrotated (geographical) coordinate system as shown in Fig. 2. Let us assume $\lambda_p = 0$. For a flow orientation parameter (or rotation angle) α the North Pole position is given by $(\lambda_p, \pi/2 - \alpha)$. The following

identities hold between the rotated (λ', φ') and unrotated (λ, φ) coordinate systems:

$$\sin \varphi' = \sin \varphi \sin \varphi_p + $$
$$\cos \varphi \cos \varphi_p \cos(\lambda - \lambda_p), \tag{2.14}$$
$$\sin \varphi = \sin \varphi' \sin \varphi_p - $$
$$\cos \varphi' \cos \varphi_p \cos \lambda', \tag{2.15}$$
$$\cos \varphi' \sin \lambda' = \cos \varphi \sin(\lambda - \lambda_p), \tag{2.16}$$

(see, e.g., Ritchie 1987). For the steady-state conditions of section 2.1.1, expressed in the unrotated (λ, φ) coordinate system, the horizontal wind components at each vertical level satisfy

$$u(\varphi) = a \cos \varphi \frac{d\lambda}{dt}, \;\; v = a \frac{d\varphi}{dt} = 0, \tag{2.17}$$

whilst the wind components in the rotated system satisfy

$$u'(\lambda', \varphi') = a \cos \varphi' \frac{d\lambda'}{dt}, \;\; v'(\lambda', \varphi') = a \frac{d\varphi'}{dt}. \tag{2.18}$$

Differentiating (2.14) with respect to time and using equations (2.17) and (2.18) gives

$$v'(\lambda', \varphi') \cos \varphi' = - \cos \varphi_p \sin(\lambda - \lambda_p) \, u(\varphi). \tag{2.19}$$

Differentiating Eqs. (2.15) and (2.16) with respect to time and manipulating the resulting equations using (2.16) - (2.19) then yields

$$u'(\lambda', \varphi') = \quad u(\varphi) \left[\cos \lambda' \cos(\lambda - \lambda_p) + \right.$$
$$\left. \sin \varphi_p \sin \lambda' \sin(\lambda - \lambda_p) \right]. \tag{2.20}$$

2.3. Procedure for computing rotated initial conditions

Suppose now that the initial conditions in sections 2.1.1 and 2.1.2 are to be expressed in the (λ', φ') coordinate system, whose North Pole is located at the point (λ_p, φ_p) of the unrotated (geographical) coordinate system (λ, φ). The steps for obtaining the initial conditions at the meshpoints (λ', φ') of the rotated system are:

1. Compute the latitude location φ using (2.15) which yields

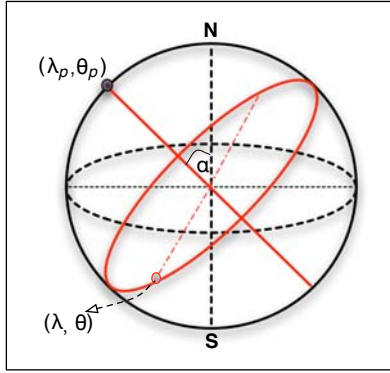$$\varphi = \arcsin \left(\sin \varphi' \sin \varphi_p - \cos \varphi' \cos \varphi_p \cos \lambda' \right) \tag{2.21}$$

Figure 2: A position (λ, θ) at the equator (dashed arrow) of a rotated coordinate system (λ', θ') whose North pole is at (λ_p, θ_p) with respect to the regular (λ, θ) sphere. N and S are the poles of the unrotated Earth and the dashed line is the equator of the unrotated coordinate system (geographical coordinates). The flow orientation parameter α (rotation angle) is the angle between the axis of the unrotated Earth and the polar axis of the rotated Earth.

2. Compute the inverse relation λ derived as

$$\lambda = \lambda_p +$$
$$\arctan\left(\frac{\cos\varphi' \sin\lambda'}{\sin\varphi \cos\varphi_p + \cos\varphi' \cos\lambda' \sin\varphi_p}\right) \quad (2.22)$$

Inverting the trigonometric functions, particularly for λ can be problematic due to the non-unique nature of the inverted $(\arctan)$ function values. To avoid this problem we recommend using the intrinsic `Fortran` function `atan2(y,x)` for $\arctan(y/x)$ which provides values in the range $[-\pi, \pi]$. The negative values between $[-\pi, 0)$ then need to be *shifted* by adding 2π. This guarantees the proper branch cut in the longitudinal direction between $[0, 2\pi]$.

3. Depending on the choice of the test case compute the zonal wind field for either the unperturbed conditions according to equation (2.2) and (2.3) or the perturbed initial conditions for the baroclinic wave test (equation 2.12). Use the results from Eqs. (2.21) and (2.22) for φ and λ. Note that the center position (λ_c, φ_c) of the perturbation in Eq. (2.11) needs to be expressed in the unrotated coordinates $(\pi/9, 2\pi/9)$.

4. Now rotate the wind vector components, that is, compute $u'(\lambda', \varphi', \eta)$ and $v'(\lambda', \varphi', \eta)$ using (2.20)

and (2.19). The (λ', φ') coordinates are the mesh-points of the computational grid. For the computation of $\cos(\lambda - \lambda')$ and $\sin(\lambda - \lambda')$ in (2.19) and (2.20) one can also use Eqs. (2.14) and (2.16) instead of (2.21) and (2.22). Equations (2.14) and (2.16) yield

$$\cos(\lambda - \lambda_p) = \frac{\sin\varphi' - \sin\varphi \sin\varphi_p}{\cos\varphi \cos\varphi_p} \quad (2.23)$$

$$\sin(\lambda - \lambda_p) = \frac{\cos\varphi' \sin\lambda'}{\cos\varphi}. \quad (2.24)$$

5. Compute the scalar fields $T'(\lambda', \varphi', \eta)$ and $(\Phi_s)'(\lambda', \varphi', \eta)$ in the rotated system by using the result of (2.21) in the temperature equation (2.5) and the expression for the surface geopotential (2.9).

This completes the definition of the rotated initial conditions for the steady-state and baroclinic wave test cases.

2.4. Test case strategy

We suggest the following test strategy for the steady-state test case. The dynamical core is initialized with the balanced initial conditions and run for 30 model days at varying horizontal resolutions and rotation angles $\alpha = 0°, 45°, 90°$.

Here we assess the convergence with resolution and the dependence of the simulated solution on the rota-

tion angle. Ideally the model results should be invariant under rotation. Any shortcomings with regard to rotation of the computational grid are due to lack of isotropy in the model. Note that a discretization scheme on an anisotropic grid can be isotropic (as is the case for the spectral transform method) and that a quasi-isotropic grid (such as the icosahedral type grids described below) not necessarily guarantees that the model dynamics is isotropic.

In addition, different horizontal resolutions should be assessed for the baroclinic wave test case to estimate the convergence characteristics. The results should also be examined as a function of rotation angle $\alpha = 0°, 45°, 90°$. The baroclinic wave starts growing observably around day 4 and evolves rapidly thereafter with explosive cyclogenesis at model day 8. The wave train breaks after day 9 and generates a full circulation in both hemispheres between day 20-30 depending on the model. Therefore the models herein are run for 15 days to capture the initial and rapid development stages of the baroclinic disturbance. As observed in JW06 the spread of the numerical solutions increases noticeably from model day 12 onwards indicating a predictability limit of the test case.

Here all models are run at two resolutions. The low resolution simulations utilize a grid spacing of approximately $2°$ at the model equator, the high resolution corresponds to a grid spacing of about $1°$ at the model equator. For the baroclinic wave test case we use 7 high-resolution reference solutions. High resolution reference solutions with different models still produce a certain spread in the solution. Therefore, we use the uncertainty of the reference solution as defined in JW06 to define convergence (see Section 4.2 for more details). When the ℓ_2 errors are below the uncertainty of the reference solutions given in JW06 the model is within the spread of the reference solutions and we can no longer term one model more accurate than another.

3. Models

Below is a brief description of the dynamical cores assessed in this paper. The corresponding model abbreviations used in this paper are listed in Table 2. The metadata for the models are given in Tables 3, 4 and 5. The definitions of the metadata entries are defined in the Appendix. The model metadata has been developed in collaboration with the Earth System Curator and Earth System Grid teams at NCAR. Models defined on three different spherical grids are considered: Regular or Gaussian latitude-longitude (Fig. 3a), cubed-sphere (Fig. 3b) and icosahedral grids (Fig. 3c). For the icosahedral class of grids one can either discretize on hexagons-pentagons or triangles. Both types of icosahedral grids are used by models in this ensemble.

3.1. Latitude-longitude grid models

The two dynamical cores defined on a regular or Gaussian latitude-longitude grid are part of NCAR's Community Atmosphere Model (CAM) version 3 (Collins et al. 2006). CAM_EUL is based on a spectral transform method on a Gaussian grid whereas the two model variants CAM_FV and CAM_ISEN are based on the Lin (2004) finite-volume approach with a floating Lagrangian coordinate in the vertical and regular latitude-longitude grid in the horizontal direction. The latter two utilize the hybrid sigma-pressure coordinates (CAM_FV) or isentropic coordinates (Chen and Rasch 2009) as their reference grids. The prognostic variables are interpolated back to the reference grid periodically (every 4-10 time steps).

The Eulerian spectral transform dynamical core CAM_EUL is based on the traditional vorticity-divergence form using the three-time-level semi-implicit Leapfrog time-stepping method. To damp the computational mode of the Leap-frog time-stepping scheme a Robert-Asselin filter (Asselin 1972) is applied which formally reduces the time-stepping scheme to first order. The horizontal approximation is based on spectral transforms and a quadratically unaliased transform grid with triangular truncation. In the vertical direction, centered finite differences are utilized. Note that the spherical harmonic functions are invariant under rotation. The horizontal resolution is referred to as T42, T85, etc. that denotes the triangular truncation with the total wave numbers 42 and 85, respectively. The corresponding Gaussian grids have 64×128 and 128×256 (latitude $\times$ longitude) grid points, resulting in a grid spacing of $\approx 2.8°$ (T42) and $\approx 1.4°$ (T85), respectively. As argued in Williamson (2008) these spectral resolutions are comparable to other grid-point based dynamical cores with mesh spacings of about $2°$ and $1°$. To control the inertial range of the total kinetic energy spectrum fourth-order linear horizontal diffusion (also referred to as hyperdiffusion) is applied to the vorticity (ζ), divergence (δ) and temperature (T). The horizontal and vertical grid staggering utilizes the Arakawa A (Arakawa and Lamb 1977)

Model abbreviations		Grid
CAM_EUL	NCAR's Eulerian spectral transform dynamical core in the Community Atmosphere Model (CAM)	Gaussian latitude-longitude
CAM_FV	NCAR's finite-volume dynamical core in the Community Atmosphere Model (CAM)	regular latitude-longitude
CAM_ISEN	same as CAM_FV but using a hybrid isentropic vertical coordinate	regular latitude-longitude
GEOS_FV_CUBED	GFDL/NASA's Goddard Earth Observing System Model (GEOS) model on a cubed-sphere grid	cubed-sphere
HOMME	NCAR's High Order Method Modeling Environment (HOMME) model	cubed-sphere
ICON	Max Planck Institute for Meteorology (MPI-M) Icosahedral Nonhydrostatic model	icosahedral (triangles)
CSU_SGM	Colorado State University's (CSU) general circulation model using a σ vertical coordinate	icosahedral (hexagons)
CSU_HYB	same as CSU_SGM but using a hybrid $\sigma - \Theta$ vertical coordinate	icosahedral (hexagons)

Table 2: List of model abbreviations (left column), affiliation/full name of the dynamical cores assessed in this paper (middle column) as well as spherical grid used by the model in question (right column). The acronym GFDL stands for NOAA's Geophysical Fluid Dynamics Laboratory in Princeton, NJ.

and Lorenz (Lorenz 1960) grid, respectively. The vertical coordinate is the traditional hybrid sigma-pressure coordinate. A-posteriori total mass and total energy fixers are applied to restore the conservation of these quantities at every time step. Details about the energy fixer can be found in Williamson et al. (2009).

CAM_FV is based on a flux-form finite-volume method that is built upon the Lin and Rood (1996) advection scheme and a CD-grid approach for the two-dimensional shallow water equations. The algorithm involves a half-time-step update on the Arakawa C grid that provides the time-centered winds to complete a full time step on the Arakawa D grid (Lin and Rood 1997). The momentum equations are expressed in their vector-invariant form. The Eulerian model design has semi-Lagrangian extensions in the longitudinal direction as documented in Lin and Rood (1996). The Lin-Rood advection scheme utilizes the monotonic Piecewise Parabolic Method (PPM, Colella and Woodward 1984) that implicitly prevents grid-scale noise in the vorticity field through the use of limiters. However, divergent modes must be controlled through the explicit application of horizontal divergence damping where the damping coefficient in CAM_FV is:

$$\nu = \frac{C\,L^2}{\Delta t}, \tag{3.1}$$

where $C = 1/128$ and $L^2 = a^2 \Delta\lambda\,\Delta\theta$. This avoids a spurious accumulation of energy at and near the grid scale. In CAM_FV second-order divergence damping is used with increasing strength near the model top. To stabilize the model a one-dimensional digital filter is applied along longitudes in the midlatitudes (approximately between $36°$ N/S to $66°$ N/S) and a Fast Fourier Transform (FFT) filter is used in the polar regions poleward of $69°$. The shallow water system is extended to a three-dimensional hydrostatic model using a floating Lagrangian vertical coordinate (Lin 2004). The levels float for a few (4-10) consecutive time steps before a vertical remapping step maps the variables back to the reference vertical levels. CAM_FV uses hybrid-sigma vertical coordinates as the reference grid. The Lin and Rood (1996) advection scheme is formulated in terms of inner and outer operators that are applied in the coordinate directions in a combination to reduce the operator-splitting error. In CAM_FV the outer operators are based on PPM, and the inner operators are first-order (upwind scheme). The stability properties of this scheme are discussed in Lauritzen (2007). More details on e.g. the time step length for a $1°$ grid spacing are listed in Table 3. Note that the PPM algorithm is formally third-order accurate in one dimension, but it reduces to a second-order advection algorithm in the chosen two-dimensional finite-

	CAM_EUL	CAM_FV/ISEN
Numerical method	spectral transform Eulerian	finite volume Eulerian with semi-Lagrangian extensions in the longitudinal direction
Spherical grid	Gaussian latitude-longitude	regular latitude-longitude
Projection	none	none
Spatial approximation	spectral, triangular truncation, quadratic transform grid	Piecewise Parabolic Method (PPM); second-order
Advection Scheme	spectral transform (dynamical core), tracers: shape-preserving semi-Lagrangian Williamson and Rasch (1989)	Lin and Rood (1996)
Conservation type	none	mass dry air
Conservation fixers	total energy, mass of dry air	total energy
Time Stepping	semi-implicit	explicit
Δt for approximately $1°$ at the equator	$600s$	$180s$
Internal resolution for Δt	T85, ≈ 156 km	#lon=360, #lat=181, ≈ 110 km
Temporal approximation	three-time level, Leapfrog, first-order due to Robert-Asselin filter (Asselin 1972)	two-time level, 2nd-order
Temporal filter	Robert-Asselin (coefficient: 0.06)	none
Explicit spatial diffusion	4th-order linear horizontal diffusion of ζ, δ, T (coefficient 1×10^{15} m^4 s^{-1}), 2nd-order diffusion near the model top	2nd-order horizontal divergence damping (see equation (3.1))
Implicit diffusion	none	1D monotonicity constraint in horizontal coordinate directions, increased diffusion near the model top (3-layer sponge) due to lower-order numerical methods
Explicit spatial filter	none	polar Fast-Fourier-Transform (FFT) filter, 3-point digital filter
Prognostic variables	$\zeta, \delta, T, \ln(p_s)$	Δp, mass-weighted θ, u, v
Horizontal staggering	co-located ζ, δ, scalars (spectral space), Arakawa A (Arakawa and Lamb 1977) in grid point space	mixed Arakawa C & D
Vertical coordinate	hybrid sigma-pressure	floating Lagrangian coordinate (interpolated to Eulerian hybrid sigma-pressure/isentropic periodically)
Vertical staggering	Lorenz grid (Lorenz 1960)	none

Table 3: Metadata for the models based on a regular latitude-longitude grid with approximately $1°$ grid spacing. ζ is the relative vorticity, δ the horizontal divergence and $\Delta p = p_{k+1/2} - p_{k-1/2}$ describes the pressure thickness of a model layer with vertical index k that is surrounded by the interface levels with half indices $k \pm 1/2$. The metadata entries are defined in the Appendix.

	HOMME	GEOS_FV_CUBED
Numerical method	spectral element Eulerian	finite volume Eulerian
Spherical grid	cubed-sphere	cubed-sphere
Projection	gnomonic (equi-angular)	gnomonic, equal-distance along cube edges (undocumented)
Spatial approximation	piecewise polynomials of degree 3	Piecewise Parabolic Method (PPM); second-order
Advection Scheme	spectral element Eulerian	Putman and Lin (2007,2009)
Conservation type	total energy, mass dry air	mass dry air
Conservation fixers	none	total energy
Time Stepping	explicit	explicit
Δt for approximately 1° at the equator	$90s$	$180s$
Internal resolution for Δt	30×30 elements per face with 4×4 Gauss-Legendre-Lobatto points within each element ($\approx$ 110 km)	90×90 cells per cubed-sphere face $\approx$ 110 km spacing
Temporal approximation	three-time level, Leapfrog, first-order due to Robert-Asselin filter	two-time level, 2nd-order
Temporal filter	Robert-Asselin (coefficient 0.05)	none
Explicit spatial diffusion	4th-order linear horizontal diffusion of u, v, T (coefficient 9.6×10^{14} m^4 s^{-1})	2nd-order and 4th-order horizontal divergence damping, increased damping near model top, external mode damping (coefficients $0.005 \times \Delta A_{min}/\Delta t$, $[0.05 \times \Delta A_{min}]^2 /\Delta t, 0.02 \times \Delta A_{min}/\Delta t$)
Implicit diffusion	none	1D monotonicity constraint in horizontal coordinate directions
Explicit spatial filter	none	none
Prognostic variables	u, v, T, p_s	Δp, mass-weighted θ, u, v
Horizontal staggering	Arakawa A (unstaggered)	mixed Arakawa C & D
Vertical coordinate	hybrid pressure-sigma	floating Lagrangian coordinate (interpolated to Eulerian hybrid sigma-pressure periodically)
Vertical staggering	Lorenz grid	none

Table 4: Same as Table 3 but for models based on cubed-sphere grids.

	ICON	CSU_SGM/HYB
Numerical method	finite difference Eulerian	finite difference Eulerian
Spherical grid	icosahedral triangular	icosahedral hexagonal
Projection	none	none
Spatial approximation	2nd-order finite-differences	3rd-order finite-differences
Advection Scheme	Ahmad el al. (2006) based on MPDATA (Smolarkiewicz and Szmelter, 2005)	Appendix B of Hsu and Arakawa (1990)
Conservation type	mass dry air	mass dry air
Conservation fixers	none	none
Time Stepping	semi-implicit (implicitness parameter is 0.7, Wan 2009)	explicit
Δt for approximately $1°$ at the equator	300 s	60 s
Internal resolution for Δt	46080 triangular cells (mass points) 69120 edges (velocity points), average mesh width $\approx$ 93 km	40962 hexagonal cells, distance between cell centers $\approx$ 120 km
Temporal approximation	3-time level, Leapfrog, first-order due to Robert-Asselin filter	4-time-level, Adams-Bashforth, 3rd-order
Temporal filter	Robert-Asselin (coefficient 0.1)	none
Explicit spatial diffusion	4th-order linear horizontal diffusion of u, v, T e-folding times 0.45h and 0.2h for $2°$ and $1°$ resolutions	none
Implicit diffusion	none	monotonicity constraint
Explicit spatial filter	none	none
Prognostic variables	u, v, T, p_s	ζ_a, δ, θ, mass (pseudo-density)
Horizontal staggering	C grid (Bonaventura and Ringler 2005)	Z grid (Randall 1994)
Vertical coordinate	hybrid sigma-pressure	pure sigma / hybrid sigma-theta (Konor and Arakawa 1997)
Vertical staggering	Lorenz grid	Charney-Philips (Konor and Arakawa 1997)

Table 5: Same as Table 3 but for models based on icosahedral grids. ζ_a is the absolute vorticity, f is the Coriolis parameter.

(a)   **(b)**   **(c)**
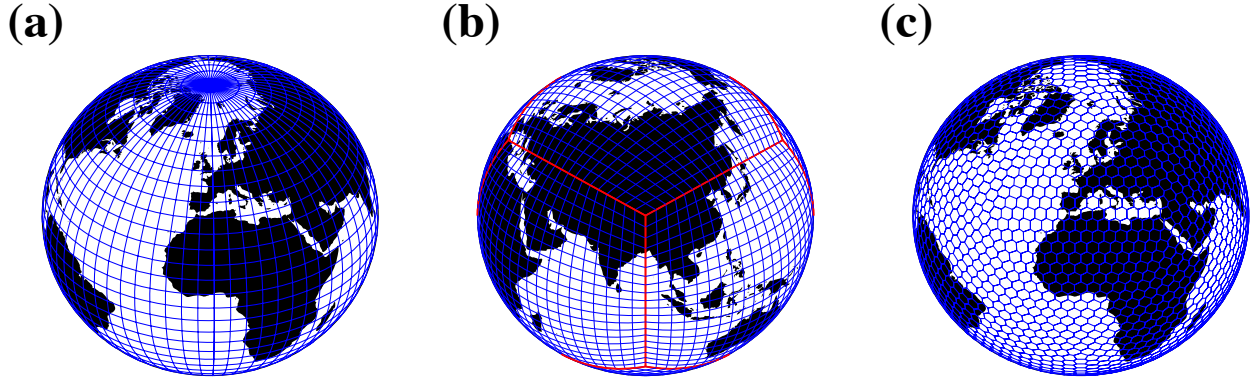
Figure 3: (a) The latitude-longitude grid, (b) the cubed-sphere grid based on an equi-angular central projection and (c) icosahedral grid based on hexagons and pentagons. The triangular grids used by models herein are the dual of the hexagonal grid.

volume implementation (i.e., the Lin and Rood, 1996, algorithm). An example of a two-dimensional extension based on the PPM algorithm that is third-order is given in, e.g., Ullrich et al. (2009).

CAM_ISEN is an isentropic version of CAM_FV. Instead of the hybrid sigma-pressure vertical coordinate a hybrid sigma-θ vertical coordinate is used (Chen and Rasch 2009). Apart from the vertical coordinate the model design is identical to CAM_FV.

3.2. Cubed-sphere grid models

The assessment includes two dynamical cores that are defined on cubed-sphere grids. The finite-volume cubed-sphere model (GEOS_FV_CUBED) is a cubed-sphere version of CAM_FV developed at the Geophysical Fluid Dynamics Laboratory (GFDL) and the NASA Goddard Space Flight Center. The advection scheme is based on the Lin and Rood (1996) method but adapted to non-orthogonal cubed-sphere grids (Putman and Lin 2007, 2009). Like CAM_FV, the GEOS_FV_CUBED dynamical core is second-order accurate in two dimensions. Both a weak second-order divergence damping mechanism and an additional fourth-order divergence damping scheme is used with coefficients $0.005 \times \Delta A_{min}/\Delta t$ and $[0.05 \times \Delta A_{min}]^2/\Delta t$, respectively, where ΔA_{min} is the smallest grid cell area in the domain.

The strength of the divergence damping increases towards the model top to define a 3-layer sponge. In contrast to CAM_FV and CAM_ISEN, the cubed-sphere model does not apply any digital or FFT filtering in the polar regions and mid-latitudes. Nevertheless, an external-mode filter is implemented that damps the horizontal momentum equations. This is accomplished by subtracting the external-mode damping coefficient ($0.02 \times \Delta A_{min}/\Delta t$) times the gradient of the vertically-integrated horizontal divergence on the right-hand-side of the vector momentum equation.

GEOS_FV_CUBED applies the same inner and outer operators in the advection scheme (PPM) to avoid the inconsistencies described in Lauritzen (2007) when using different orders of inner and outer operators. The cubed-sphere grid is based on central angles. The angles are chosen to form an equal-distance grid at the cubed-sphere edges (undocumented). The equal-distance grid is similar to an equidistant cubed-sphere grid that is explained in Nair et al. (2005). The resolution is specified in terms of the number of cells along a panel side. As an example, 90 cells along each side of a cubed-sphere face yield a global grid spacing of about $1°$.

The second cubed-sphere dynamical core is NCAR's spectral element High-Order Method Modeling Environment (HOMME) (Thomas and Loft 2004, Nair et al. 2009). Spectral elements are a type of a continuous-Galerkin h-p finite element method (Karniadakis and Sherwin 1999, Canuto et al. 2007), where h is the number of elements and p the polynomial order. Rather than using cell averages as prognostic variables as in geos_fv_cubed, the finite element method uses p-order polynomials to represent the prognostic variables inside each element. The spectral element method is *compatible*, meaning it has discrete analogs of the key integral properties of the divergence, gradient and curl operators, making the method elementwise mass-conservative (to
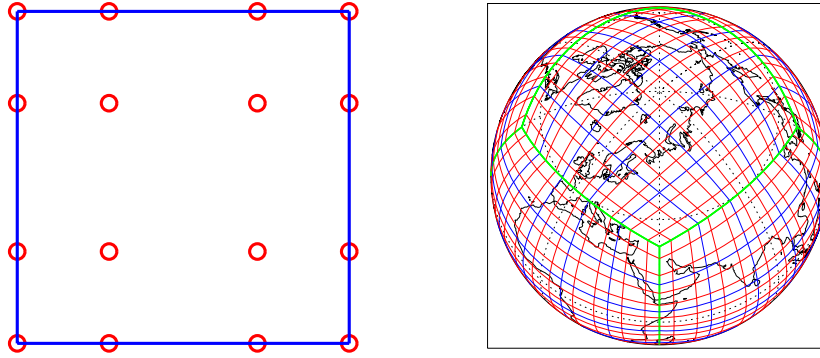
Figure 4: (left) A graphical illustration of the Gauss-Legendre-Lobatto quadrature points (red unfilled circles) in an element (blue boundary) of the HOMME model. (right) The mapping of every element onto the sphere. Green lines are the boundary of the cubed-sphere faces.

machine precision) and total energy conservative (to the truncation error of the time-integration scheme) (Taylor et al. 2007, Taylor et al. 2008). The cubed-sphere grid consists of elements with boundaries defined by an equiangular gnomonic grid (Nair et al. 2005) and each element has $(p+1) \times (p+1)$ Gauss-Legendre-Lobatto quadrature points. The positions of the Gauss-Legendre-Lobatto quadrature points in each element are depicted in Fig. 4. For the simulations presented here $p = 3$ is used and the resolution is determined by h, the number of elements along a face side. The grid spacing at the equator is approximately $90°/(h * p)$ hence the approximately $1°$ solutions use $h = 30$ and $p = 3$. The model applies fourth-order linear horizontal diffusion to the prognostic variables u, v and T. The diffusion coefficient is tuned empirically with the help of kinetic energy spectra as done in CAM_EUL.

3.3. Icosahedral grid models

Two icosahedral-grid based models are tested with three model variants. Among them is the model *ICON* that is under development at the Max-Planck Institute for Meteorology, Germany, and the German Weather Service DWD. Some documentation on ICON is given in Wan (2009). The second model labeled *CSU* has been developed at the Colorado State University, Fort Collins, U.S.. Here two model variant of *CSU* are assessed that use different vertical coordinates. The icosahedral grids are special types of geodesic grids where an icosahedron inscribed in a sphere is subdivided recursively to form a quasi-uniform grid of triangles. In the CSU model the

grid resolution is specified in terms of the number of refinement levels of the icosahedron that initially consists of 20 triangles. Each refinement level subdivides the mesh, thereby doubling its resolution. The hexagonal grid is the dual of the triangular grid. It is created by connecting the centroids of the triangles sharing a vertex with great circle arcs. It consists primarily of hexagons and 12 pentagons. If ℓ is the number of bisections of an original icosahedral edge the number of hexagonal grid cells is given by

$$2 + 10 \times 4^{\ell}. \qquad (3.2)$$

A resolution of approximately $1°$ is obtained with $\ell = 6$ (40962 cells) corresponding to a minimum and maximum grid point distance between the cell centers of 110 km and 132 km, respectively. The number of triangles in this grid is given by

$$20 \times 4^{\ell} \qquad (3.3)$$

which corresponds to 81920 triangles for $\ell = 6$. Note that the ICON results discussed in this paper are based on a slightly different distribution of the triangular grid cells. The main difference is the initial refinement strategy for the icosahedron. Instead of bisecting the grid, the original icosahedron is first split by a factor of three along each edge before further recursive bisections are introduced. If $m = \ell - 2 = 4$ is the number of bisections after the initial 3-way split the number of triangular cells n_c, triangle edges n_e and triangle vertices n_v is then

given by

$$n_c = 20 \times 3^2 \times 4^m \qquad (3.4)$$
$$n_e = 30 \times 3^2 \times 4^m \qquad (3.5)$$
$$n_v = 10 \times 3^2 \times 4^m + 2. \qquad (3.6)$$

For the approximately $1°$ triangular grid with $m = 4$, 46080 triangular cells with 69120 edges and 23042 vertices result in an average mesh width of 93 km. One can either use the hexagons (pentagons) or triangles as control volumes for the discretization. The icosahedral grids give an almost homogeneous and quasi-isotropic coverage of the sphere. The hexagonal grid has a somewhat higher degree of symmetry than triangular grids whereas triangular grids are more straight forward to refine if mesh refinement is desired. Both icosahedral grid models (CSU and ICON) optimize the icosahedral grid so that the truncation error for the spatial finite-difference operators is guaranteed to converge to zero as the grid-cell sizes decrease to zero. See Heikes and Randall (1995) for more details.

In this study, we use a development version of the ICON (Icosahedral Nonhydrostatic) dynamical core that utilizes the triangular control volumes. Although the model abbreviation refers to a non-hydrostatic model, the version used here is based on the hydrostatic equation set in vector-invariant form. The model applies 2nd-order finite-difference approximations on an Arakawa C horizontal grid (Bonaventura and Ringler 2005) and a Lorenz grid in the vertical. The velocity reconstruction algorithm is based on Radial Basis Functions (RBF). The vertical coordinate is the hybrid sigma-pressure coordinate. The time-stepping algorithm is semi-implicit using an implicitness parameter of 0.7 (see Wan 2009). The computational mode of the three-time-level Leapfrog time-stepping scheme is damped with a Robert-Asselin filter. The advection scheme is MPDATA (Smolarkiewicz 1983; Smolarkiewicz and Szmelter 2005) adapted to the icosahedral grid (Ahmad el al. 2006). Efforts are ongoing to develop a higher-order advection scheme for ICON (A. Gassman, personal communication 2009). Fourth-order linear horizontal diffusion is applied to u, v, T along the model levels. The time steps used for the $1°$ (46080 cells) and $2°$ (11520 cells) runs are 300 s and 600 s, respectively. It should be noted that the ICON model is undergoing rapid development (partly due to the experience with the test case suite run during the NCAR ASP 2008 summer colloquium). Hence, the results presented here are with an older version of ICON.

The CSU dynamical core is based on hexagons (and 12 pentagons). The model directly predicts vorticity and divergence. Stream function and velocity potential are obtained by solving elliptic equations using multigrid methods. The vorticity and divergence are co-located at cell centers following the Z-grid (Randall 1994) that provides attractive linear dispersion properties for, e.g., geostrophic adjustment and has no computational modes. A four-time-level third-order Adams-Bashforth time-integration method is used for mass (pseudo-density), θ, absolute vorticity ζ_a, and divergence δ. The advection scheme of the CSU model is described in Appendix B of Hsu and Arakawa (1990). Two options for the vertical coordinates are used in these tests. One is the traditional pure sigma coordinate (CSU_SGM) while the other is a hybrid sigma-theta vertical coordinate (Konor and Arakawa 1997) referred to as CSU_HYB. The vertical staggering is an equivalent Charney-Philips staggering (Konor and Arakawa 1997). Monotonicity constraints in the advection operator (flux-corrected transport, Zalesak 1979) may produce implicit diffusion. The time steps for the $1°$ (40962 cells) and $2°$ (10242 cells) grid spacings are 60 s and 120 s, respectively.

4. Results

To facilitate data handling and model comparisons the output for each model was interpolated to a regular latitude-longitude grid. In the model HOMME the *interpolation* was performed by evaluating the internal basis functions at the regular latitude-longitude grid points. CSU_SGM and CSU_HYB use area-weighted interpolation and GEOS_FV_CUBED use bilinear interpolation. For the baroclinic wave test case, the ℓ_2-error for a particular model are computed by interpolating the non-rotated high-resolution reference solution (CAM_EUL at T340 resolution) to the regular latitude-longitude grid to which the native model data has been interpolated.

4.1. Rotated steady-state test case

The steady-state test case measures the model's ability to maintain a steady-state solution and its sensitivity to the rotation of the grid while keeping the physical flow the same. For simplicity the test is evaluated in terms of the surface pressure field which avoids vertical interpolations to pressure levels. No new insights are found when assessing other variables like T, u, v, ζ, δ. Figure 5 shows the p_s field in model coordinates (not geographical coordinates) at day 1 for models based on reg-

ular latitude-longitude and cubed-sphere grids with the approximately 2° horizontal resolution. The figures also show some of the grid lines of the computational grid as well as selected wind vectors at model level 3 near 14 hPa. The wind vectors show the locations of the jets in the model's coordinate system. The computational grid lines illustrate how the grid impacts the numerical solution (discussed separately below for each model). Note that the contours for p_s are not the same for all plots. Figure 6 is the same as Fig. 5 but for the icosahedral-grid based models.

In addition to model day 1 we also show the surface pressure fields at day 9 when the grid effects are more pronounced. Model day 9 is depicted in Figs. 7 and 9 that show the dynamical cores based on regular latitude-longitude and cubed-sphere grids at approximately 2° and 1° horizontal resolutions, respectively. A common contour interval is used. Results for the icosahedral grid models are presented in Figs. 8 and 10. The steady-state test has an analytic solution (p_s=1000 hPa) that allows the computation of root mean square ℓ_2 error. The ℓ_2 error for the regular latitude-longitude and cubed-sphere grids are shown in Fig. 11. Figure 12 depicts the time series of the surface pressure error for the icosahedral-hexagonal models. The definition of the ℓ_2-error is provided in JW06. Each figure is discussed in greater detail below.

The three-dimensional steady-state flow is baroclinically and barotropically unstable due to its horizontal and vertical shear characteristics, hence any perturbation introduced into the flow will grow. Due to the basic mechanisms in baroclinic instability the flow is more sensitive to perturbations introduced around the midlatitudes near the latitudinal position of the jets in contrast to, for example, perturbations introduced at the equator.

Depending on the rotation angle when ℓ_2 grows to a value somewhere in the interval $]0.2, 0.4[$ hPa the spurious waves start growing exponentially. We define (somewhat arbitrarily) $\ell_2 = 0.5$ hPa as the threshold value after which a model is termed unable to maintain a balanced flow. At that point the amplitude of the spurious waves has grown beyond approximately 0.5 hPa and grows exponentially. Note that the same conclusions could be drawn by using any threshold value larger than approximately 0.3 hPa (and less than approximately 8 hPa).

4.1.1. Regular latitude-longitude grid models

The unrotated results of the regular latitude-longitude models show that the numerical schemes maintain the balances in the flow for at least 30 days (left column in Fig. 11). However, when the computational grid is rotated so that the flow is no longer aligned with the grid lines, spurious waves start growing early during the simulation. In case of CAM_FV and CAM_ISEN (Fig. 5) noisy patterns appear in the surface pressure fields by day 1. The spurious waves have larger amplitudes for $\alpha = 45°$ than for $\alpha = 90°$. For $\alpha = 45°$ the jets cross the poles of the computational grid (Fig. 1). Numerical approximations near the poles such as filtering, averaging, etc., trigger a wave train in each hemisphere similar to the wave train triggered by the boundaries in the limited-area model of Lauritzen et al. (2008). In their case however, the growing wave was triggered by the boundary relaxation scheme and elliptic solver in the boundary zone.

For $\alpha = 90°$ the poles of the computational grid are at the equator and hence far away from the baroclinically most unstable region located in the mid-latitudes. Hence less accurate approximations in the polar regions of the computational grid are not the main trigger for spurious waves rather the fact that the grid lines predominantly are at an angle with respect to the jets (see, e.g., Fig. 1). In fact the angle between the jet maximum and the computation grid latitudes is approximately 45° in four locations and less than 45° elsewhere. The numerical approximations tend to be most accurate for flow aligned with grid lines (angle between jet and computational latitudes $\approx 0°$) and least accurate for traverse flow (angle between jet and computational latitudes $\approx 45°$). This seems to trigger the wavenumber four pattern apparent in the surface pressure fields of the two finite volume models at day 9 (Fig. 7, right column).

The growth of the baroclinic wave is slightly stronger in CAM_ISEN than in CAM_FV. When doubling the horizontal resolution similar results are obtained (Figs. 7 and 9). Nevertheless, the growth of the spurious waves is delayed by approximately two days (Fig. 11) at the higher resolution. This is expected since higher resolutions reduce the numerical truncation errors.

For CAM_EUL the results at day 9 at low and high resolutions (Figs. 7 and 9) appear to be invariant under rotation. This might be expected due to the fact that a triangular truncation of spherical harmonics is invariant under rotation. However, the ℓ_2-error in Fig. 11 reveal that the rotated versions of CAM_EUL cannot maintain a balanced initial state throughout the 30-day integration. At about day 19 and 26 the rotated versions of CAM_EUL lose the symmetry at the 2° and 1° resolutions, respectively. It is speculated that the spurious wave is triggered

because the spherical harmonic functions do not represent the initial conditions exactly.

4.1.2. Cubed-sphere models

Both cubed-sphere models HOMME and GEOS_FV_CUBED show a distinct wavenumber 4 grid imprint in the surface pressure field at day 9 at the coarse 2° resolution (Fig. 7, last two rows). The grid imprint appears in each hemisphere for $\alpha = 0°$ and $\alpha = 90°$. The corners of the cubed-sphere in each hemisphere are located near the centers of the jets for $\alpha = 0°$ and $\alpha = 90°$, thereby positioning them in the baroclinically most unstable regions. This is depicted in Fig. 5 that shows the cubed-sphere panel-side outline and the position of the jets. The discretizations tend to have the largest errors near the corners of the inscribed cube. Since these are near the baroclinically most unstable regions, the wavenumber 4 spurious wave is induced into the circulation and grows fast. The amplitude of the spurious wave is larger in GEOS_FV_CUBED than in HOMME. This is most likely due to the high-order numerical scheme and consistent finite-element-based treatment of the corners in HOMME. There is some indication that the Putman and Lin (2007) advection scheme introduces additional errors, in particular near the edges, due to its dimensional split characteristics as explained in the next paragraph.

In the challenging moving vortices advection test case of Nair and Jablonowski (2008) the convergence rates for the Lauritzen et al. (2009) scheme is approximately one order of magnitude higher than for the Putman and Lin (2007) scheme. Both schemes use the same order of reconstruction function so the only major difference between the two schemes is that the Lauritzen et al. (2009) scheme is fully two-dimensional, in particular it uses a rigorous fully two-dimensional treatment of the corners of the cube, whereas the Putman and Lin (2007) scheme uses a dimensional split approach. This seems to indicate that the dimensional split approach has a less accurate treatment of the corners of the cubed-sphere as compared to other approaches.

GEOS_FV_CUBED can no longer maintain the steady-state at approximately day 6 and 12 for the 2° and 1° resolution (Fig. 11). Hence, doubling the horizontal resolution delays the break-down of the steady-state by 6 days which is a large improvement compared to most other models. This could indicate that GEOS_FV_CUBED is below its minimal recommendable resolution at a 2° grid spacing. The model HOMME can maintain the steady-state for 16 and 18 days at the coarse and fine resolutions.

In the $\alpha = 45°$ case (Fig. 11, middle column) we observe that the performance of the models degrade and the break-down of the steady-states occurs approximately 2 days earlier in comparison to $\alpha = 0°, 90°$ (apart from GEOS_FV_CUBED at 2° resolution). The wave signature in the surface pressure field has an overlaid wavenumber 2 and wavenumber 4 characteristic rather than a pure wavenumber 4 imprint as seen before (Figs. 7 and 9). The following reasons are suggested. At the $\alpha = 45°$ rotation angle the flanks of the jets traverse two vertices rather than four (Fig. 5). This triggers the wavenumber 2 error signature that overlays the wavenumber 4 background error. In addition, the advection operators tend to be more accurate when the flow is quasi-parallel to coordinate lines which is predominantly the case for $\alpha = 0°$ and $\alpha = 90°$. At the $\alpha = 45°$ rotation angle the flow mostly traverse the coordinate lines at an angle, thereby triggering enhanced errors as also discussed in Lauritzen (2007).

4.1.3. Icosahedral models

Similar to the corners of the cubed-sphere grid and the pole points of the regular latitude-longitude mesh, the hexagonal-icosahedral grids have 12 pentagons that usually require special attention in the model discretizations. The triangular-hexagonal grids show the largest deviations from their almost uniform grid spacings near the dual-grid pentagons. This triggers a distinct and expected wavenumber 5 grid imprint in the icosahedral-grid based models in the non-rotated case (Fig. 8). The spurious wave trains in the Northern and Southern atmosphere are offset by 36° degrees due to the relative location of the pentagons in the two hemispheres (Fig. 8 and 10). Note that the pentagons are located near the maximum intensity of the jets (Fig. 6) where the flow is baroclinically most unstable. The model ICON already shows the wavenumber 5 pattern at day 1.

In the rotated cases it is less clear how the numerical discretizations near the pentagons adversely affect the solution. For $\alpha = 45°$ and $\alpha = 90°$ the locations of the pentagons in each hemisphere of the computational domain are not symmetric since (regular) hexagons have symmetry properties for 60° rather than 45° and 90°. This triggers the asymmetric response in the surface pressure field in all icosahedral simulations at the rotation angles $\alpha = 45°$ and 90° (Fig. 8 and 10, middle and right column). At the 1° resolution (Fig. 10) the amplitudes of the growing spurious waves in ICON

are largest at the $\alpha = 45°$ rotation angle, whereas they are largest at the $90°$ angle in the models CSU_HYB and CSU_SGM. All three icosahedral model variants improve their representation of the steady-state at the higher resolution. The ICON model can maintain the steady-state solution the shortest. It breaks down after approximately 8 and 10 days at the $2°$ and $1°$ resolutions, respectively. The steady-states in the high-resolution versions of CSU_SGM and CSU_HYB break down after approximately 12 days whereas the lower resolution version differs by a day (Fig. 12). The CSU_HYB model variant with the hybrid isentropic vertical coordinate shows that the spurious perturbations introduced by the numerics grow slightly faster than the perturbations in the traditional sigma-pressure model version. A similar observation was made for the CAM_FV and CAM_ISEN model pair.

4.2. Rotated baroclinic wave test case

As for the steady-state test case we consider the surface pressure at day 9 with three rotation angles ($\alpha = 0°, 45°, 90°$) and the two $2°$ and $1°$ resolutions. The figures for surface pressure are grouped as before for the steady-state test case. In particular, the surface pressure field at the low resolution for the regular latitude-longitude and cubed-sphere grid based models are shown in Fig. 13. The icosahedral-grid based models are depicted in Fig. 14. The plots zoom in on the main wave train in the northern hemisphere. The corresponding plots for the high $1°$ resolution runs are presented in Figs. 15 and 16. Since the relative vorticity fields for this test case contain more fine-scale structures than the surface pressure we also show the 850 hPa relative vorticity (see Figs. 17, 18, 19 and 20). Finally, the l_2 surface pressure error for non-icosahedral and icosahedral grid based models are presented in Figs. 21 and 22 at approximately $2°$, respectively, and similarly for the $1°$ solutions on Figs. 23 and 24.

To compute the l_2-errors a reference solution is needed as no analytical solution is known for the baroclinic wave test case. Here we use all high-resolution reference solutions available (at $0.25°$ resolution) to compute l_2-errors. These are GEOS_FV_CUBED, CAM_EUL (T340 truncation), CAM_FV, HOMME, CSU_SGM as well as the reference solutions used in JW06 that are not part of our model suite: CAM_SLD and GME which are a semi-Lagrangian version of CAM_EUL and a finite-difference icosahedral (hexago-

nal) model developed at the DWD, respectively (for more details see JW06). JW06 used four models (CAM_EUL, CAM_SLD, CAM_FV, GME) to define the uncertainty of the reference solutions based on the argument that by increasing the resolution beyond $0.25°$ one does not get a better estimate of the 'true' solution. This is illustrated on JW06's Figure 10 in that increasing the resolution from approximately $0.5°$ to $0.25°$ the differences in l_2-errors between the models does not decrease. The maximum difference in l_2-error between any two models and any of the $0.5°$ and $0.25°$ resolutions defines the uncertainty of the reference solutions. Our model ensemble is larger than the four models used in JW06 and one could argue that the spread in the model solutions could increase by using more models. However, by computing the l_2-errors between all $0.25°$ reference solution models for which we have data, all l_2-errors are within the uncertainty of the JW06 ensemble (see Fig. 25) and we therefore find it adequate to use the JW06 uncertainty estimate (yellow regions on Fig. 21, 22, 23, 24).

We use the following terminology regarding convergence of models to within the uncertainty of the reference solutions: If all l_2-errors based on all available reference solutions are outside the yellow region, we term the model *non-converged* at that particular resolution. And similarly, if all l_2-errors based on all available reference solutions are in the yellow region, we term the model *converged* at that particular resolution. If none of the above, some reference solutions produce l_2 errors inside the yellow area and some outside, the model is termed *converging* (tend to convergence) in the sense that the model has started to converge but higher resolution is needed to term the model *converged* with higher fidelity. As noted by JW06 the initial phase of the wave growth (0-6 days) is easily dominated by interpolation errors and the predictability of the test is approximately 12 days. So the terminology regarding convergence applies to the time span from approximately 6 to 12 days.

4.2.1. Regular latitude-longitude models

The CAM_EUL model exhibits relatively little variation of the surface pressure evolution with rotation angle at both low and high resolution. Nevertheless, Fig. 13 shows a slight indication that the development of the baroclinic wave in CAM_EUL is less strong in the rotated versions of the test at approximately $2°$ resolution. This becomes even clearer in the relative vorticity field in Fig. 17. However, at the higher resolution (Figs. 15 and 19) the observed anisotropy in the solution is drasti-

cally reduced and CAM_EUL has converged at the high resolution.

Overall, CAM_FV and CAM_ISEN show the same behavior but with a generally less strong baroclinic development in terms of the highs and lows in the wave train. This observation is confirmed in the error measures in Fig. 23 where the approximately $1°$ runs with CAM_FV and CAM_ISEN are converging but have not converged. At the $1°$ resolution the differences between the unrotated and rotated model experiments is larger for the CAM_FV and CAM_ISEN models than for the spectral transform model. The observation that CAM_FV and CAM_ISEN need higher resolution for convergence in this test case has also been demonstrated in more complex simulations with physical parameterizations. For example, Williamson (2008) showed in so-called aqua-planet experiments (Neale and Hoskins 2000) that CAM_FV needs a higher horizontal resolution to *match* the CAM_EUL results in terms of a wide range of diagnostics.

4.2.2. Cubed-sphere models

The cubed-sphere models perform very similarly and show little dependence on rotation angle. At the approximately $2°$ resolution the deep low in surface pressure at day 9 is slightly deeper for the rotated cubed-sphere runs than for the corresponding CAM_EUL run (Fig. 13). At high resolution CAM_EUL and the cubed-sphere models show almost identical p_s fields (Fig. 15). This indicates that the cubed-sphere models have converged as is confirmed in the l_2 error measures in Fig. 23. There is a slight indication in the l_2 error that for $\alpha = 45°$ the solutions are slightly less accurate than for the other rotation angles. In fact GEOS_FV_CUBED at $\alpha = 45°$ is on the verge to be termed converging rather than converged. Also, the relative vorticity fields show some slight variation with rotation angle at both low and high resolution for the cubed-sphere models (Fig. 17 and 19). This is most likely due to the flow being predominantly traverse to grid cells at $\alpha = 45°$. In contrast the flow is predominantly parallel to the grid lines for $\alpha = 0°$ and $\alpha = 90°$.

4.2.3. Icosahedral models

Among the icosahedral models the ICON model shows large variation in surface pressure and relative vorticity fields under the rotation of the computational grid. This is especially apparent at the low $2°$ resolution (Fig. 14).

At the higher $1°$ resolution the dependence of the solution on the rotation angle strongly decreases (Fig. 16). It suggests that the minimal recommendable resolution for the ICON model is higher than approximately $2°$. However, even at the $1°$ resolution the relative vorticity field for ICON still shows relatively large variation with rotation angle (Fig. 20).

The CSU_SGM and CSU_HYB models show fewer variations with rotation angle but differences are visible in the surface pressure field for the low resolution runs (Fig. 14). The deep low of the wave train is strongest for $\alpha = 90°$ contrary to the regular latitude-longitude models that had the strongest baroclinic developments for the non-rotated version of the test case. This dependence on rotation angle practically disappears at higher resolution as can be seen in both the p_s field (Fig. 16) and the 850 hPa relative vorticity fields (Fig. 20). The CSU_HYB model based on isentropic vertical coordinates has a stronger baroclinic development than its conventional vertical coordinate counterpart (CSU_SGM). The l_2 error shows that CSU_HYB is on the verge of being termed convergent at approximately $1°$ resolution whereas the CSU_SGM is not. In fact CSU_SGM is non-convergent at the high resolution. Note that even in the steady-state test case the spurious perturbations grew faster in the isentropic vertical coordinate version of the model in comparison to the hybrid sigma-pressure model variant (Fig. 12). It is unknown whether this characteristic is due to a slightly inaccurate initialization (e.g. introduced by interpolations) or a general property of the isentropic vertical coordinate models.

5. Conclusions

In this paper a rotated version of the Jablonowski steady-state and baroclinic wave test case for dry dynamical cores of GCMs has been introduced. The underlying idea is to rotate the computational grid with respect to the physical flow to eliminate any symmetries between the grid and the flow field. Models based on regular latitude-longitude grids are somewhat favored by the unrotated version of the Jablonowski test case since the flow is predominantly zonal and thereby aligned with the grid lines. This makes it less challenging for regular latitude-longitude grid based models to maintain the balance in the steady-state test. Other grid configurations such as cubed-sphere and icosahedral meshes do not exhibit any zonal symmetries. Therefore, they are more challenged to maintain the zonally symmetric balance. However,

these non-traditional grids provide a more uniform grid coverage on the sphere. Their variation of the grid cell area is small in comparison to regular latitude-longitude grids with converging meridians. It is therefore expected that they only exhibit weak dependencies on the rotation angle when displacing the computational grid poles from the geographical poles.

The rotated steady-state and baroclinic wave test case were tested by a wide variety of global dynamical cores that participated in a dynamical core intercomparison. The latter was part of the NCAR ASP 2008 summer colloquium that evaluated the characteristics of 12 dynamical cores at large scales. Here we present results of six models with eight model variants. The models represent a wide spectrum of numerical schemes and computational grids like regular latitude-longitude grids, cubed-sphere meshes and icosahedral grids. Among them are the four dynamical cores that are part of the NCAR Community Atmosphere Model CAM: CAM_EUL, CAM_FV, CAM_ISEN and HOMME. In addition we present results from the CSU models CSU_HYB, CSU_SGM, the newly developed MPI model ICON as well as the GFDL/NASA dynamical core GEOS_FV_CUBED on the cubed-sphere grid. We focus on the simulations with the two horizontal resolutions $1°$ and $2°$ (at the model equator) and three rotation angles $0°, 45°, 90°$.

First, the ability to maintain a balanced steady-state flow field was examined as a function of rotation angle and resolution. Since the flow is baroclinically unstable any perturbation will eventually grow and result in spurious waves. After reaching a certain threshold level the spurious waves grow exponentially. We term a particular model unable to maintain a balanced flow when the l_2 surface pressure errors increase beyond a certain threshold level, here set to $\ell_2 = 0.5$ hPa. The number of days a model retains a balanced flow field as a function of resolution and rotation angle was examined. For the models defined on different grids we found different spurious forcings, also referred to as *grid imprinting*. The *grid imprinting* depends on the rotation angle, the relative latitudinal location of the jets, which are also the baroclinically most unstable regions, and the strong/weak singularities of the underlying spherical grid. As expected, unrotated versions of the steady-state test case developed a wavenumber 4 pattern for cubed-sphere models and a wavenumber 5 pattern for models based on an icosahedral grid. When rotating the grid at the $45°$ angle the cubed-sphere models developed an overlaid wavenum-

ber 2 and 4 pattern. The wavenumber 2 occurs since the flanks of the jet now traverse two corners of the cubed-sphere grid rather than four in this configuration. The icosahedral models have symmetry properties for a $60°$ rotation angle rather than $45°$. Therefore, the icosahedral models show an asymmetric response under the $45°$ and $90°$ rotation. Assuming that the growth rates for the spurious waves are equal in all respective models, the strength of the grid imprinting is proportional to the breakdown of the steady-state. The times of the breakdown vary significantly among the models and rotation angles. At the $1°$ and $2°$ resolutions they varied between 6 - 26 days.

For the rotated versions of the baroclinic wave test case the surface pressure and 850 hPa relative vorticity at day 9 were examined. In addition, the l_2 surface pressure errors were computed for all models using 7 high resolution reference solutions. The l_2 errors indicate the resolution at which the models converge to within the uncertainty of the high-resolution reference solutions (as defined in JW06). We term a model *converged* when l_2 based on all reference solutions are within the uncertainty of the reference solutions and *non-converged* when all l_2 errors are outside. If some of the l_2-errors are outside and some inside the uncertainty region we term the model *converging* in the sense that the model has started to converge but higher resolution is needed to term the model *converged* with higher fidelity.

All models were non-converged at the lower $2°$ resolution and they showed large variation with rotation angle. At the high $1°$ resolution most models show a decrease in (or almost no) dependence on the rotation angle in terms of p_s, the relative vorticity and l_2 errors. The models CAM_EUL, HOMME and GEOS_FV_CUBED were converged at $1°$ grid spacing and CSU_HYB was on the verge of being termed converged. CAM_FV and CAM_ISEN were converging at the high resolution but slightly higher resolution is needed to be termed converged. CSU_HYB and ICON were non-convergent and therefore need higher resolution for convergence.

We argue that this test case is a useful tool for debugging model code and for model development in general when evaluating the anisotropy in the solutions with various grid systems. For example, the cubed-sphere model runs should be identical for the non-rotated and $90°$ rotation angles because of the symmetry properties of the grid. In addition, the impact of filtering and numerical discretizations near the (weak) singularities can be readily assessed with this test case. It also provides a simple

framework to estimate the minimal recommended resolutions to simulate large scale baroclinic instability. It is largely unknown how the spurious grid forcing (grid imprinting) is impacting full model simulations with physical parameterizations. For example, the paleo-climate community models at low resolution (relatively speaking) mainly due to limitations in computing power. The grid imprinting at low resolutions could potentially be a problem in long runs if its magnitude is comparable to the physical forcings in the system. More research in this area is needed. The test cases presented herein give an indication of the magnitude of the grid forcing in a short term simulation.

In this study, we did not attempt to compute an effective resolution of each model, e.g. the resolution needed to hold a steady state for some fixed number of days. Nor did we compare the relative computational cost between the different models, e.g. we did not compute the ratio between accuracy versus computational cost. Since some models were highly optimized for the computer used during the NCAR ASP colloquium and others were not, it was found *unfair* to try and compare computational cost. Also, in the light of massive parallel computing the performance of a model at low processor count as used during the colloquium may be very different in comparison to massive processor usage. Our main goal was not to rank models but rather to demonstrate the usefulness of the test in model development. Obviously, good performance in an idealized test case does not guarantee superior performance when coupled to the full physics package or run at fine scales. However, if a model show excessive spurious grid forcing and is unable to maintain large scale balances in the flow, it would be questionable if such a model would be adequate for long term simulations, especially at coarse climate resolutions.

Appendix: Definition of metadata

The definitions of the metadata entries used in Tables 3, 4 and 5 are given below:

Numerical method: The basic numerical method used to discretize the equations of motion (excluding tracer transport). Examples are finite-difference, finite-volume, spectral element or spectral transform methods. In addition, the Eulerian or semi-Lagrangian formulation of the equations is denoted. Note that a combinations of the numerical methods are used in some models.

Projection: Any projection used for the discretization of the equations of motion. For example, cubed-sphere grids can use gnomonic (equiangular) or gnomonic (equal-distance along cube edges). Also, planar projections used in some icosahedral grid models etc.

Spatial approximation: Spatial approximations used for the discretization of the equations of motion. The formal order of accuracy is denoted. Examples are second-order finite-differences, finite-volume with polynomial subgrid distributions (e.g. the piecewise parabolic method PPM). Note that some models use different classes of spatial approximations for different variables.

Advection Scheme: Scheme used to approximate the advective operator in the equations of motion as well as for tracers. Examples are the Lin and Rood (1996) scheme, spectral transform, MPDATA (Smolarkiewicz and Szmelter 2005), etc. Note that some models use a different scheme for the advection operator in the equa-

tions of motion than for tracers.

Conservation type: Physical characteristics of the equations of motion that are conserved by the numerical discretization. For example, mass of dry air, total energy.

Conservation fixers: Any physical quantities that are formally conserved by the continuous equations of motion and restored with an a-posteriori fixer in the dynamical core (due to non-conservation in the numerical schemes). For example, dry air mass, total energy.

Time Stepping: Time stepping used in the schemes used to discretize the equations of motion. For example, explicit, implicit, semi-implicit.

Δt *for approximately 1° at the equator:* Time step size Δt used for running the model at approximately 1° at the model equator.

Internal resolution for Δt: Horizontal resolution used in the model corresponding to the Δt given above. The resolution is specified in terms of internal representation of resolution used in the model. For example, 90x90 cells per cubed-sphere face (approximately 110 km grid spacing), T85 spectral resolution (approximately 156 km), #lon=360 #lat=181 for the regular latitude-longitude grid (approximately 110 km).

Temporal approximation: The temporal approximation used in the time-stepping method for advancing the equations of motion forward in time. It is specified in terms of number of time-levels, name of scheme (if applicable, with reference) and order of accuracy. For example, three-time-level Leapfrog (formally second-order, order reduced if filtered), two-time-level (second-order accurate), four-time-level Adams-Bashforth (third order accurate).

Temporal filter: Any filters applied to the time-stepping method to remove spurious waves. For example, Robert-Asselin (Asselin 1972).

Explicit spatial diffusion: Any explicit diffusion terms added to the equations of motion. For example, 4th order linear horizontal diffusion, 2nd order divergence damping.

Implicit diffusion: Implicit diffusion is inherent diffusion in the numerical schemes not enforced through the addition of diffusion operators in the equations of motion. For example, monotonicity constraints in the sub-grid-cell reconstruction function, FCT (flux corrected transport), off-centering.

Explicit spatial filter: Filtering that is applied in space that is not implemented in terms of explicit diffusion operators and implicit diffusion. For example, FFT filtering, digital diltering, Shapiro filter.

Prognostic variables: Prognostic variables used in the discretizations of the equations of motion. For example, (u,v,T,p_s), (vorticity, divergence, potential temperature, surface pressure).

Horizontal staggering: Staggering used in the horizontal. For example, Arakawa A, B, C or D (Arakawa and Lamb 1977).

Vertical coordinate: Vertical coordinate used in the discretizations of the equations of motion. For example, hybrid sigma-pressure, sigma, hybrid sigma-theta (isentropic). Some models use a combination of Eulerian and Lagrangian vertical coordinates, that is, an initial Eulerian vertical coordinate evolves as a Lagrangian surface for a number of time-steps and is then periodically remapped back to an Eulerian reference vertical coordinate (Lin 2004, Nair et al. 2009).

Vertical staggering: Staggering used in the vertical. For example, Lorenz (Lorenz 1960) staggering.

References

Ahmad, N. N., D. P. Bacon, M. S. Hall, and A. Sarma, 2006: Application of the multidimensional positive definite advection transport algorithm (MPDATA) to environmental modelling on adaptive unstructured grids. *Int. J. Numer. Meth. Fluids,* **50**, 1247-1268. DOI: 10.1002/fld.1113

Arakawa, A., and V. R. Lamb, 1977: Computational design of the basic dynamical processes of the UCLA general circulation model. *Methods Comput. Phys.,* **17**, 173-265.

Asselin, R., 1972: Frequency Filter for Time Integrations. *Mon. Wea. Rev.,* **100**, 487-490.

Bonaventura, L., and T. Ringler, 2005: Analysis of Discrete Shallow-Water Models on Geodesic Delaunay Grids with C-Type Staggering. *Mon. Wea. Rev.,* **133**, 2351-2373. DOI: 10.1175/MWR2986.1

Chen, C.-C., and P. Rasch, 2009: Climate Simulations with an Isentropic Finite Volume Dynamical Core. *J. Climate*, submitted.

Colella, P., and P. R. Woodward, 1984: The Piecewise Parabolic Method (PPM) for gas-dynamical simulations. *J. Comput. Phys.*, **54**, 174-201. DOI: 10.1016/0021-9991(84)90143-8

Collins, W. D., P. J. Rasch, B. A. Boville, J. J. Hack, J. R. Mc-Caa, D. L. Williamson, B. P. Briegleb, C. M. Bitz, S.-J. Lin, and M. Zhang, 2006: The Formulation and Atmospheric Simulation of the Community Atmosphere Model Version 3 (CAM3). *J. Climate*, **19**, 2144-2161. DOI: 10.1175/JCLI3760.1

Canuto, C. G., M. Y. Hussaini, A. Quarteroni, and T. A. Zang, 2007: *Spectral Methods: Evolution to Complex Geometries and Applications to Fluid Dynamics (Scientific Computation)*. Springer, 598 pp.

Galewsky, G., R. K. Scott, and L. M. Polvani, 2004: An initial-value problem for testing numerical models of the global shallow-water equations. *Tellus*, **56**, 429-440. DOI: 10.1111/j.1600-0870.2004.00071.x

Heikes, R., and D. A. Randall, 1995: Numerical Integration of the Shallow-Water Equations on a Twisted Icosahedral Grid. Part II. A Detailed Description of the Grid and an Analysis of Numerical Accuracy. *Mon. Wea. Rev.*, **123**, 1881-1887. DOI: 10.1175/1520-0493(1995)123<1881:NIOTSW>2.0.CO;2

Hsu, Y. J. G., and A. Arakawa, 1990: Numerical Modeling of the Atmosphere with an Isentropic Vertical Coordinate. *Mon. Wea. Rev.* **118**, 1933-1959. DOI: 10.1175/1520-0493(1990)118<1933:NMOTAW>2.0.CO;2

Jablonowski, C, 2004: Adaptive Grids in Weather and Climate Modeling, Ph.D. Thesis, University of Michigan, Ann Arbor, MI, USA, 2004, 292 pp.

Jablonowski, C, P. H. Lauritzen, M. A. Taylor, and R. D. Nair, 2009: Idealized test cases for the dynamical cores of Atmospheric General Circulation Models. *Geoscientific Model Development*, in prep. http://esse.engin.umich.edu/admg/publications.php

Jablonowski, C., and D. L. Williamson, 2006a: A baroclinic instability test case for atmospheric model dynamical cores. *Quart. J. Roy. Meteor. Soc.*, **132**, 2943-2975. DOI: 10.1256/qj.06.12

Jablonowski, C., and D. L. Williamson, 2006b: A baroclinic wave test case for dynamical cores of general circulation models: Model intercomparisons. *NCAR Technical Note*, **NCAR/TN-469+STR**, 75 pp.

Karniadakis, G. E., and S. J. Sherwin, 1999: Spectral/Hp Element Methods for CFD. 408pp. ISBN-13: 9780195102260

Konor, C. S., and A. Arakawa, 1997: Design of an Atmospheric Model Based on a Generalized Vertical Coordinate. *Mon. Wea. Rev.*, **125**, 1649-1673. DOI: 10.1175/1520-0493(1997)125<1649:DOAAMB>2.0.CO;2

Lauritzen, P. H., 2007: A Stability Analysis of Finite-Volume Advection Schemes Permitting Long Time Steps. *Mon. Wea. Rev*, **135**, 2658-2673. DOI: 10.1175/MWR3425.1

Lauritzen, P. H., E. Kaas, B. Machenhauer, and K. Lindberg, 2008: A mass-conservative version of the semi-implicit semi-Lagrangian HIRLAM. *Quart. J. Roy. Meteor. Soc.*, **134**, 1583-1595. DOI: 10.1002/qj.307

Lauritzen, P. H., R. D. Nair, and P. A. Ullrich, 2009: A conservative semi-Lagrangian multi-tracer transport scheme (CSLAM) on the cubed-sphere grid. *J. Comput. Phys.*, in press. DOI: 10.1016/j.jcp.2009.10.036.

Läuter, M., D. Handorf, and K. Dethloff, 2005: Unsteady analytical solutions of the spherical shallow water equations, *J. Comput. Phys.*, **210**, 535-553. DOI: 10.1016/j.jcp.2005.04.022.

Lin, S.-J., 2004: A 'Vertically Lagrangian' Finite-Volume Dynamical Core for Global Models. *Mon. Wea. Rev.*, **132**, 2293-2307. DOI: 10.1175/1520-0493(2004)132<2293:AVLFDC>2.0.CO;2

Lin, S.-J., and R. B. Rood, 1996: Multidimensional flux-form semi-Lagrangian transport schemes. *Mon. Wea. Rev.*, **124**, 2046-2070. DOI: 10.1175/1520-0493(1996)124<2046:MFFSLT>2.0.CO;2

Lin, S.-J., and R. B. Rood, 1997: An explicit flux-form semi-lagrangian shallow-water model on the sphere. *Quart. J. Roy. Meteor. Soc.*, **123**, 2477-2498. DOI: 10.1002/qj.49712354416

Lorenz, E. N., 1960: Energy and numerical weather prediction. *Tellus.*, **12**, 364-373

Machenhauer, B., E. Kaas, and P. H. Lauritzen. 2008: Finite-Volume Methods in Meteorology. *Computational Methods for the Atmosphere and the Oceans, Special Volume*, **14**, 784 pp., ISBN-13: 978-0-444-51893-4

Nair, R. D., H. W. Choi, and H. M. Tufo, 2009: Computational aspects of a scalable high-order discontinuous Galerkin atmospheric dynamical core. *Computers & Fluids*, **30**, 309-319. DOI: 10.1016/j.compuid.2008.04.006

Nair, R. D., and C. Jablonowski, 2008: Moving Vortices on the Sphere: A Test Case for Horizontal Advection Problems. *Mon. Wea. Rev.*, **136**, 699-711. DOI: 10.1175/2007MWR2105.1

Nair, R. D., S. J. Thomas, and R. D. Loft, 2005: A discontinuous Galerkin Transport Scheme on a Cubed Sphere. *Mon. Wea. Rev.*, **133**, 814-828.

Neale, R. B., and B. J. Hoskins, 2000: A standard test for AGCMs including their physical parametrizations: I: the

proposal. *Atmospheric Science Letters*, **1**, 101-107. DOI: 10.1006/asle.2000.0022

Phillips, N. A., 1957: A coordinate system having some special advantages for numerical forecasting. *J. Meteorol.*, 14, 184-185.

Polvani, L. M., R. K. Scott, and S. J. Thomas, 2004: Numerically Converged Solutions of the Global Primitive Equations for Testing the Dynamical Core of Atmospheric GCMs. *Mon. Wea. Rev.*, **132**, 2539-2552. DOI: 10.1175/MWR2788.1

Putman, W. M., and S.-J. Lin, 2007: Finite-volume transport on various cubed-sphere grids. *J. Comput. Phys.*, **227**, 55-78. DOI: 10.1016/j.jcp.2007.07.022.

Putman, W. M., and S.-J. Lin, 2009: A finite-volume dynamical core on the cubed-sphere grid. *Numerical Modeling of Space Plasma Flows: Astronum-2008*, *Astronomical Society of the Pacific Conference Series*, **406**, 268-276.

Randall, D. A., 1994: Geostrophic Adjustment and the Finite-Difference Shallow-Water Equations. *Mon. Wea. Rev.*, **122**, 1371-1377. DOI: 10.1175/1520-0493(1994)122<1371:GAATFD>2.0.CO;2

Ritchie, H., 1987: Semi-Lagrangian Advection on a Gaussian Grid. *Mon. Wea. Rev.*, **115**, 608-619. DOI: 10.1175/1520-0493(1987)115<0608:SLAOAG>2.0.CO;2

Simmons, A., and D. Burridge, 1981: An Energy and Angular-Momentum Conserving Vertical Finite-Difference Scheme and Hybrid Vertical Coordinates. *Mon. Wea. Rev.*, **109**, 758-766. DOI: 10.1175/1520-0493(1981)109<0758:AEAAMC>2.0.CO;2

Smolarkiewicz, P. K., 1983: A Simple Positive Definite Advection Scheme with Small Implicit Diffusion. *Mon. Wea. Rev.*, **111**, 479-486. DOI: 10.1175/1520-0493(1983)111<0479:ASPDAS>2.0.CO;2

Smolarkiewicz, P. K., and J. Szmelter, 2005: MPDATA: An edge-based unstructured-grid formulation. *J. Comput. Phys.*, **206**, 624-649.

Staniforth, A., and A. A. White, 2008a: Stability of some exact solutions of the shallow-water equations for testing numerical models in spherical geometry. *Quart. J. Roy. Meteor. Soc.*, **134**, 771-778. DOI: 10.1002/qj.240

Staniforth, A., and A. A. White, 2008b: Unsteady exact solutions of the flow equations for three-dimensional spherical atmospheres. *Quart. J. Roy. Meteor. Soc.*, **134**, 1615-1626. DOI: 10.1002/qj.300

Staniforth, A., and A. A. White, 2008c: A generalized thermal wind equation and some non-separable exact solutions of the flow equations for three-dimensional spherical atmospheres. *Quart. J. Roy. Meteor. Soc.*, **134**, 1931-1939. DOI: 10.1002/qj.323

Taylor, M. A., J. Edwards, S. Thomas, and R. D. Nair, 2007: A mass and energy conserving spectral element atmospheric dynamical core on the cubed-sphere grid. *J. Phys. Conf. Ser.*, **78**, 012074. DOI: 10.1088/1742-6596/78/1/012074

Taylor, M. A., J. Edwards, and A. St-Cyr, 2008: Petascale Atmospheric Models for the Community Climate System Model: New Developments and Evaluation of Scalable Dynamical Cores. *J. Phys. Conf. Ser.*, **125**, 012023. DOI: 10.1088/1742-6596/125/1/012023

Thomas, S. J., and R. D. Loft, 2005: The NCAR Spectral Element Climate Dynamical Core: Semi-Implicit Eulerian Formulation. *J. Sci. Comput.*, **25**, 307–322. DOI: 10.1007/s10915-004-4646-2

Ullrich, P. A., C. Jablonowski, and B. van Leer, 2010: Riemann-solver-based high-order finite-volume models for the shallow-water equations on the sphere. *J. Comput. Phys.*, in review.

Wan, H., 2009: Developing and testing a hydrostatic atmospheric dynamical core on triangular grids, *Reports on Earth System Science*, Max-Planck Institute for Meteorology, Hamburg, Germany, **65**, pp. 153, ISSN 1614-119

Wedi, N. P., and P. K. Smolarkiewicz, 2009: A framework for testing global non-hydrostatic models. *Quart. J. Roy. Meteor. Soc.*, **135**, 469-484. DOI: 10.1002/qj.377

Williamson, D. L., 2008: Equivalent finite volume and Eulerian spectral transform horizontal resolutions established from aqua-planet simulations. *Tellus*, **60**, 839-847. DOI: 10.1111/j.1600-0870.2008.00340.x

Williamson, D. L., J. B. Drake, J. J. Hack, R. Jakob, and P. N. Swarztrauber, 1992: A standard test set for numerical approximations to the shallow water equations in spherical geometry. *J. Comput. Phys.*, **101**, 227-228. DOI: 10.1016/0021-9991(92)90060-C

Williamson, D. L. and J. Olson, and C. Jablonowski, 2009: Two Dynamical Core Formulation Flaws Exposed by a Baroclinic Instability Test. *Mon. Wea. Rev.*, **137**, 790-796.

Williamson, D. L., and P. J. Rasch, 1989: Two-dimensional semi-Lagrangian transport with shape preserving interpolation. *Mon. Wea. Rev.*, **117**, 102-129.

Zalesak, S., 1979: Fully multidimensional flux-corrected transport algorithms for fluids. *J. Comput. Phys.*, **31**, 335-362. DOI: 10.1016/0021-9991(79)90051-2

Zerroukat, M, N. Wood, and A. Staniforth, 2005: A monotonic and positive-definite filter for a Semi-Lagrangian Inherently Conserving and Efficient (SLICE) scheme. *Quart. J. Roy. Meteor. Soc.* **131**, 2923-2936. DOI: 10.1256/qj.04.97

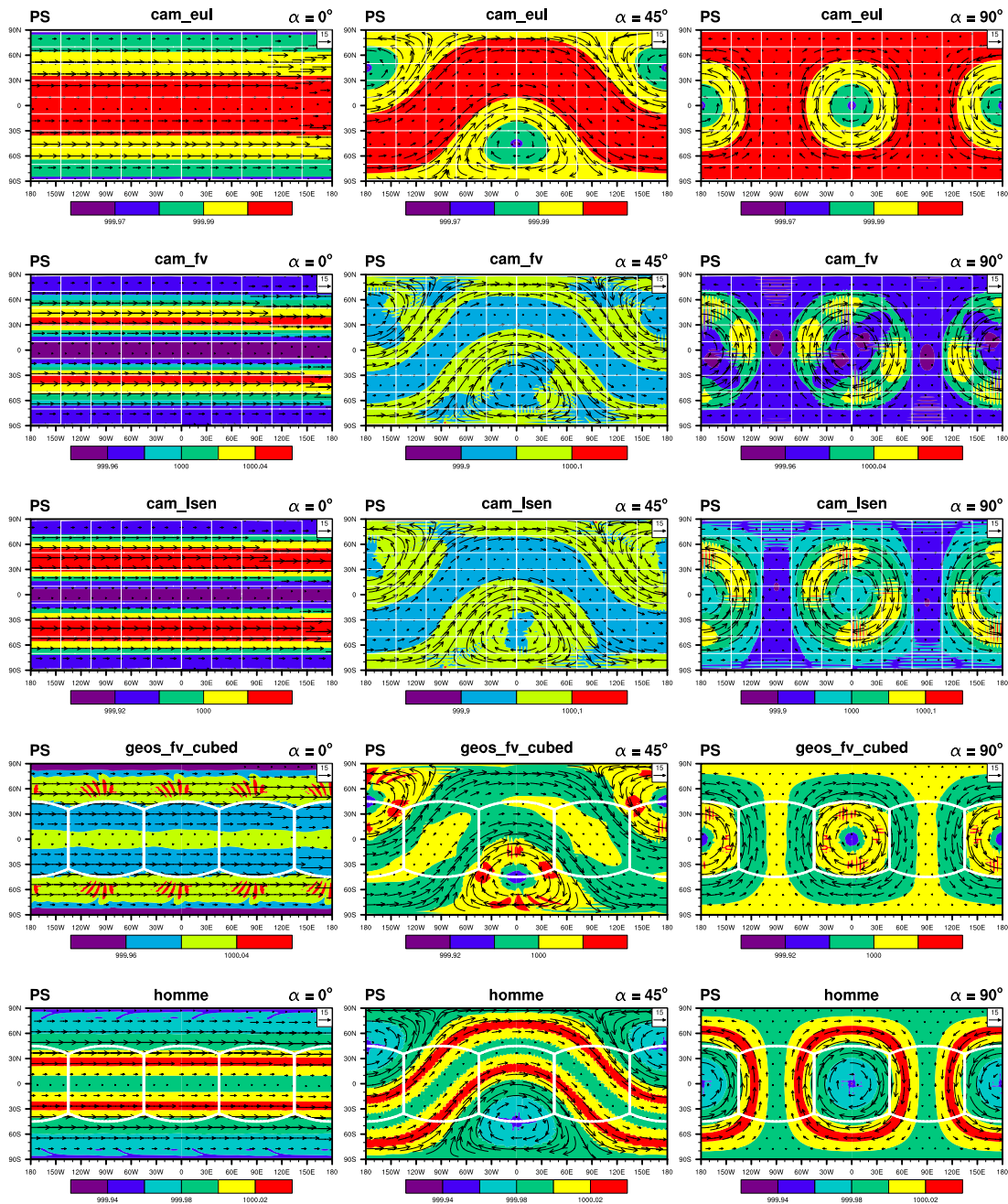Day 1, approximately 2° horizontal resolution at equator

Figure 5: Surface pressure (hPa) at day 1 in model coordinates (not geographical coordinates) for models based on regular latitude-longitude and cubed-sphere grids at approximately 2° horizontal resolution at rotation angles $\alpha = 0°$ (left column), $\alpha = 45°$ (middle column) and $\alpha = 90°$ (right column). The figures also show some of the grid lines for the computational grid (white solid lines) as well as the vector wind field at model level 3 near 14 hPa for the initial condition (the offset in the wind vectors around 120E in the first column reflects a plotting problem rather than a change in the zonal winds). The wind vectors are only shown to indicate the location of the jets with respect to the model grid. Each plot has different color contouring. The model abbreviation is above each plot (see also Table 2).

JAMES-D
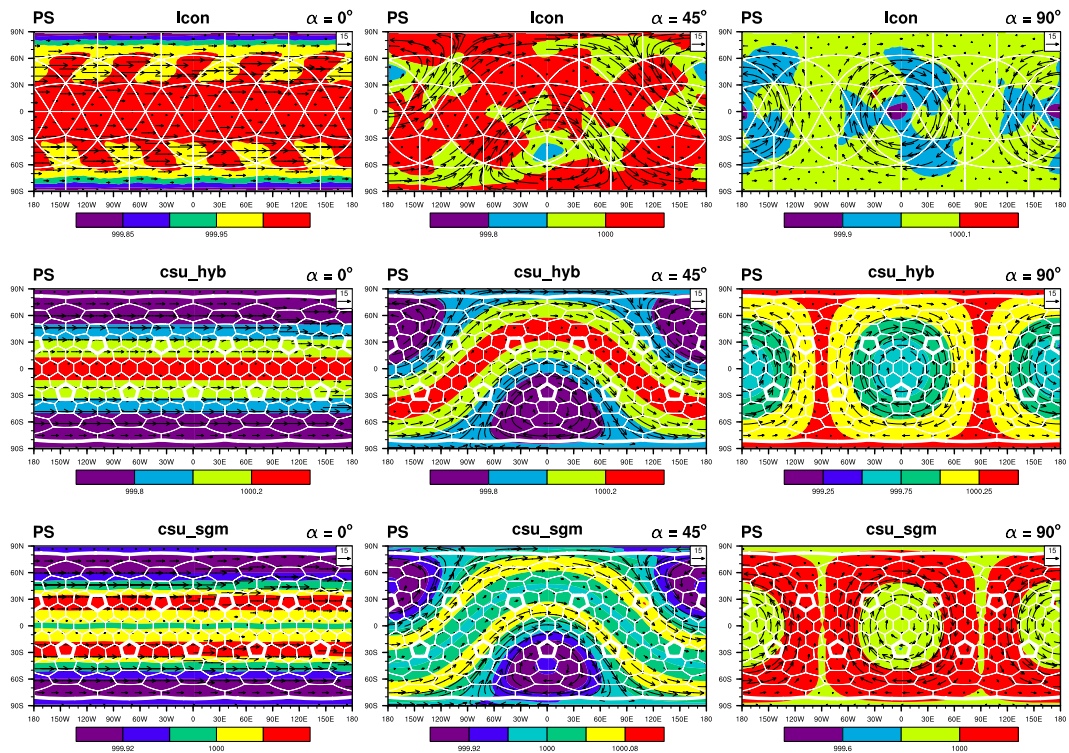
Figure 6: Same as Fig. 5 but for the icosahedral grid models at day 1. The pentagons of the hexagon grid are marked with thick white lines.

Day 9, approximately 2° horizontal resolution at equator
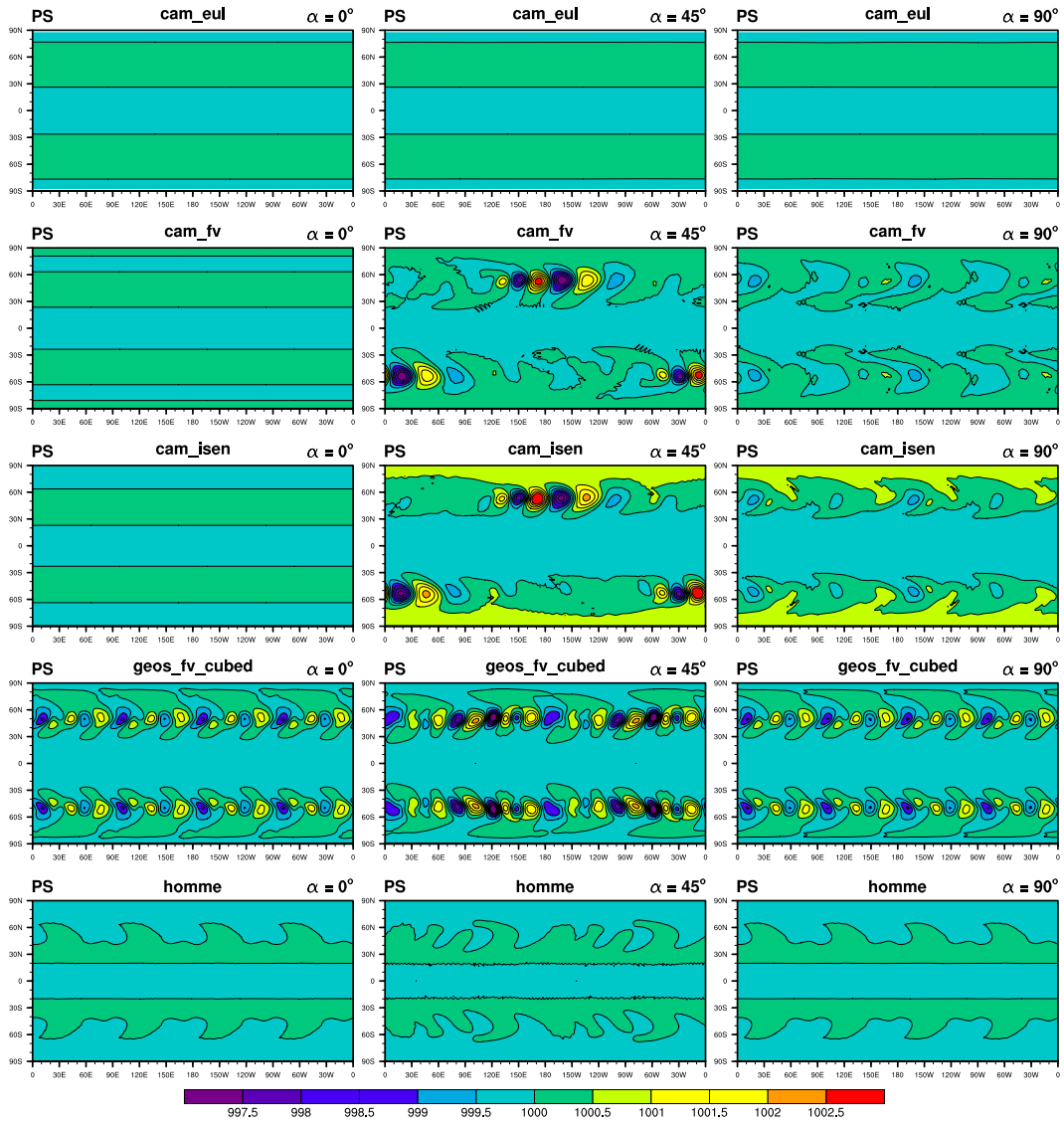
Figure 7: Surface pressure (hPa) at day 9 for models based on a regular latitude-longitude and cubed-sphere grids for different rotation angles (left, middle and right columns are $\alpha = 0°, 45°$ and $90°$, respectively). The models use a grid spacing of $\approx 2°$.
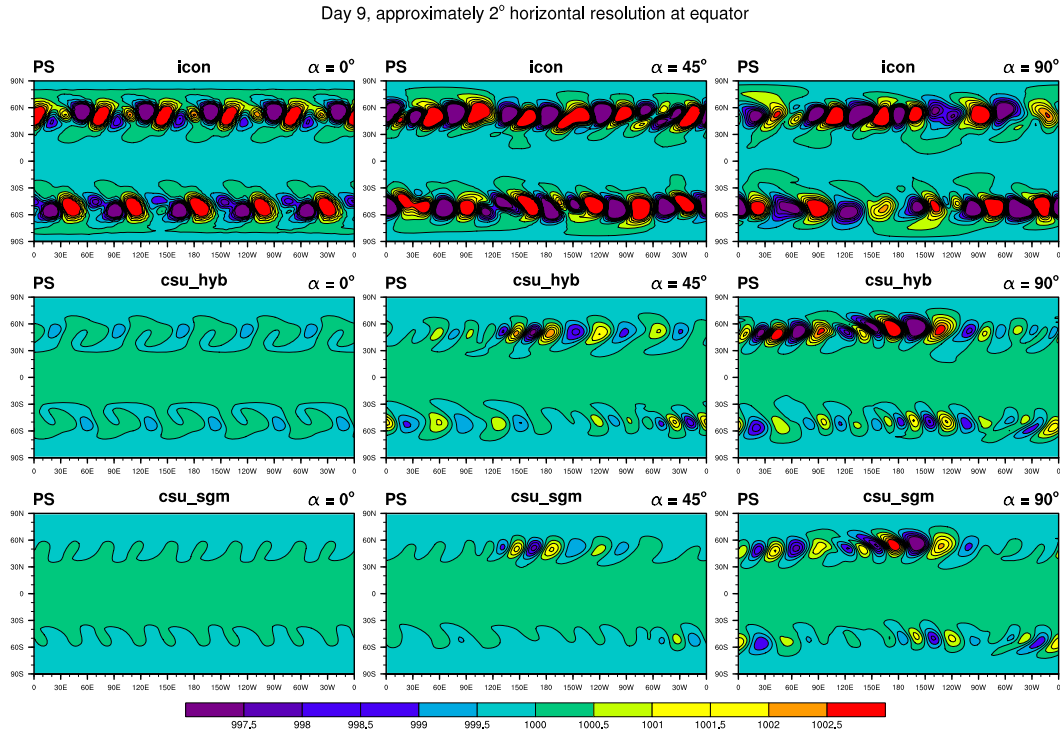
Figure 8: Same as Fig. 7 but for the icosahedral grid models at day 9. To faciliate the visual comparison of p_s among the models the contour interval is from 997.5 hPa to 1002.5 hPa. Obviously the contours for p_s for ICON, CSU_HYB and CSU_SGM go beyond this range (the full range for ICON is approximately from 992 hPa to 1004 hPa).

Day 9, approximately 1° horizontal resolution at equator
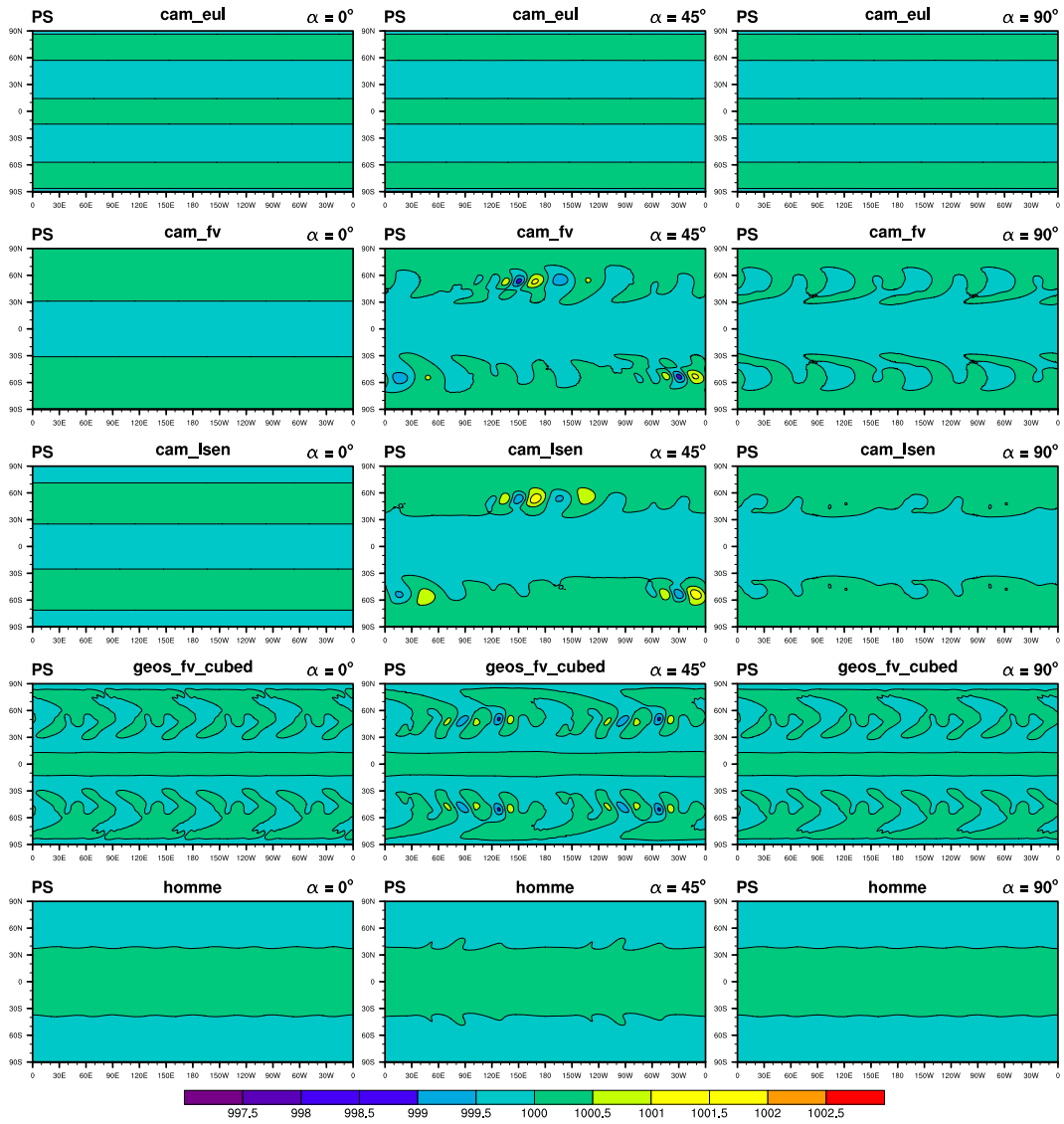
Figure 9: Same as Fig. 7 but for a grid spacing of $\approx 1°$.
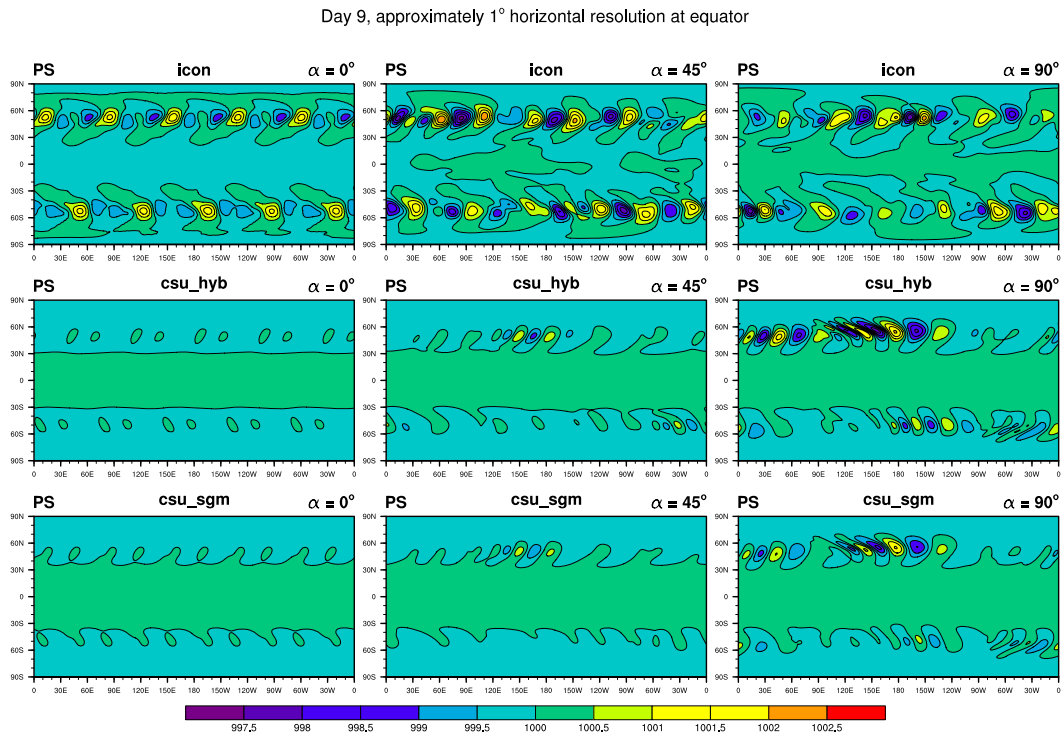
Figure 10: Same as Fig. 9 but for models based on an icosahedral grid.
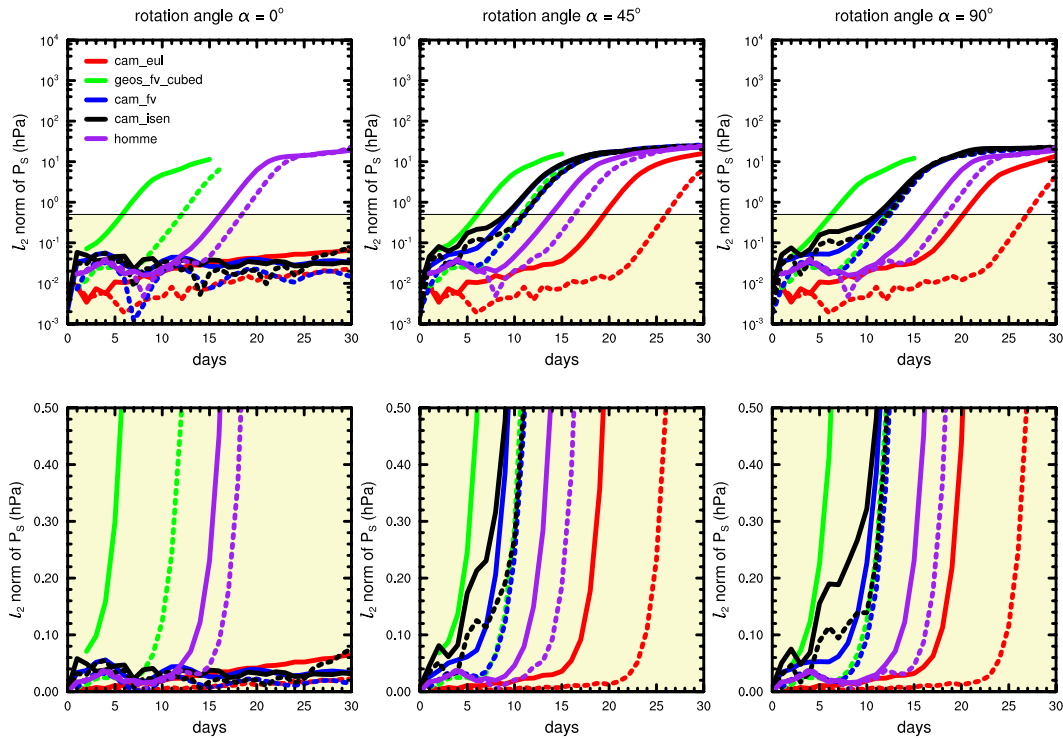
Figure 11: Time series of the root mean square ℓ_2-errors (in hPa) for dynamical cores defined on regular latitude-longitude and cubed-sphere grids using rotation angles (left column) $0°$, $45°$ (middle column) and $90°$ (right column), respectively. The model abbreviations are defined in Table 2. Solid and dashed lines are for horizontal grid spacings of $\approx 2°$ and $\approx 1°$, respectively. In the upper row the y-axis is on a logarithmic scale and in the lower row the y-scale is linear. The yellow region marks the $\ell_2 < 0.5$ hPa region.
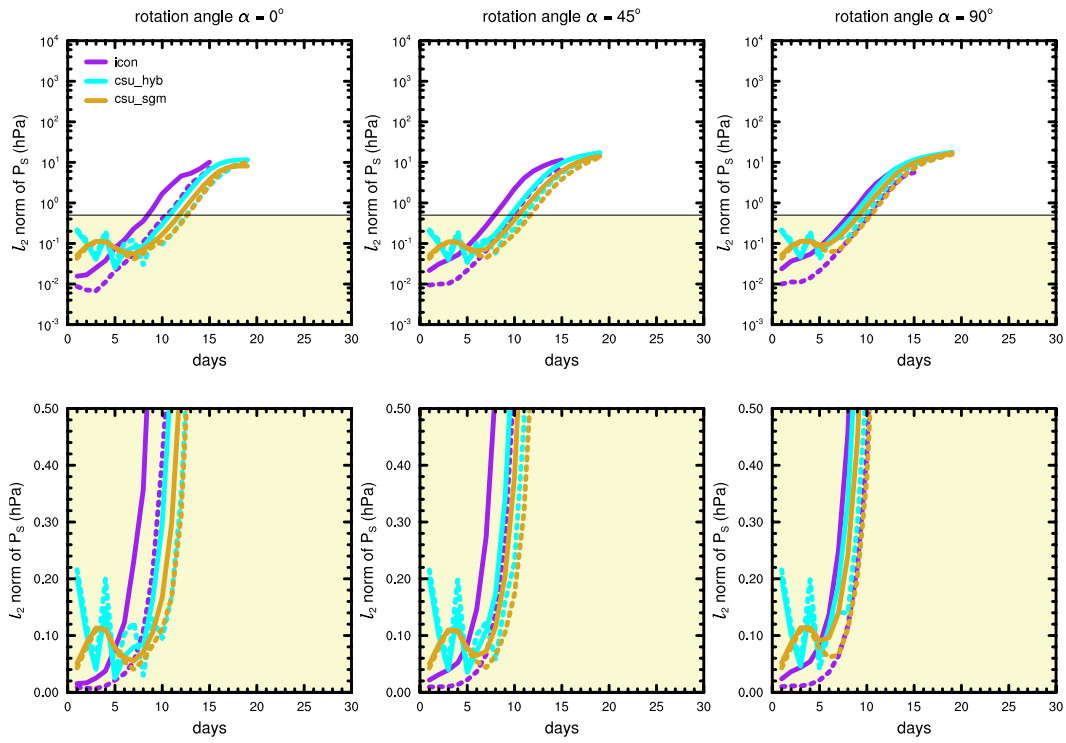
Figure 12: Same as Fig. 11 but for models defined on icosahedral grids.

Day 9, approximately 2° horizontal resolution at equator
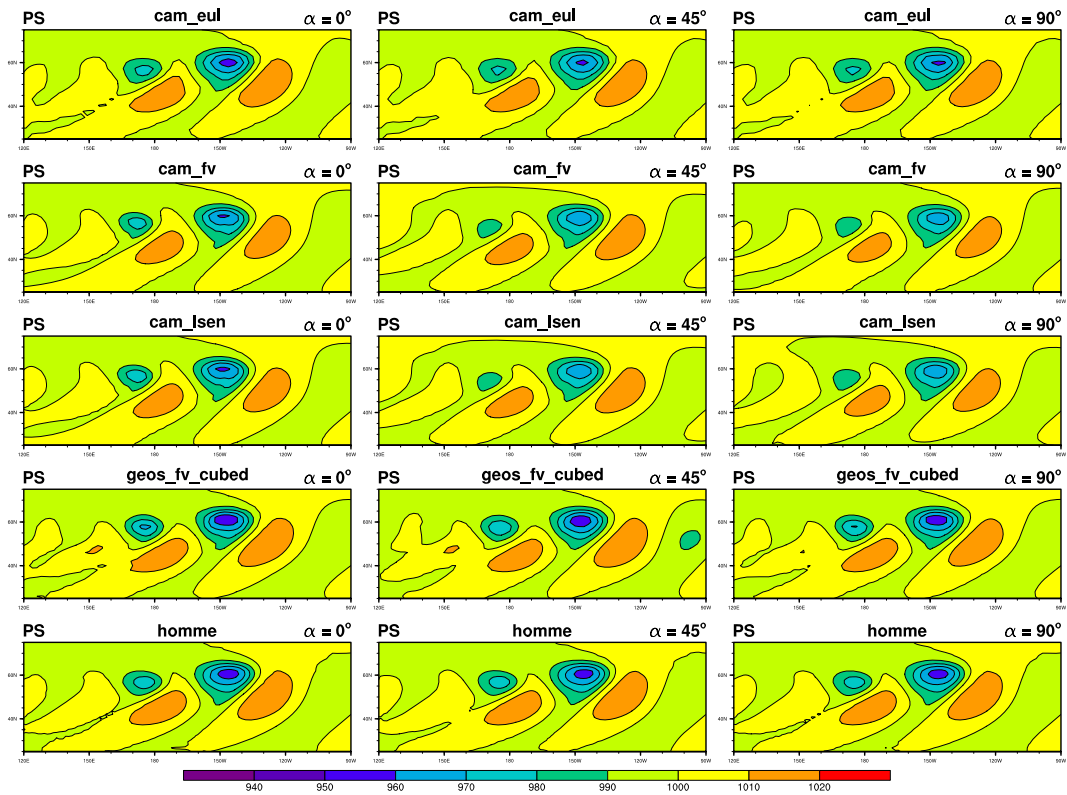
Figure 13: Surface pressure (hPa) at day 9 for the baroclinic wave test case for models based on a regular latitude-longitude and cubed-sphere grids for different rotation angles (left, middle and right columns are $\alpha = 0°, 45°$ and $90°$, respectively). The grid spacing is $\approx 2°$. The plots zoom into the baroclinic wave.

Day 9, approximately 2° horizontal resolution at equator
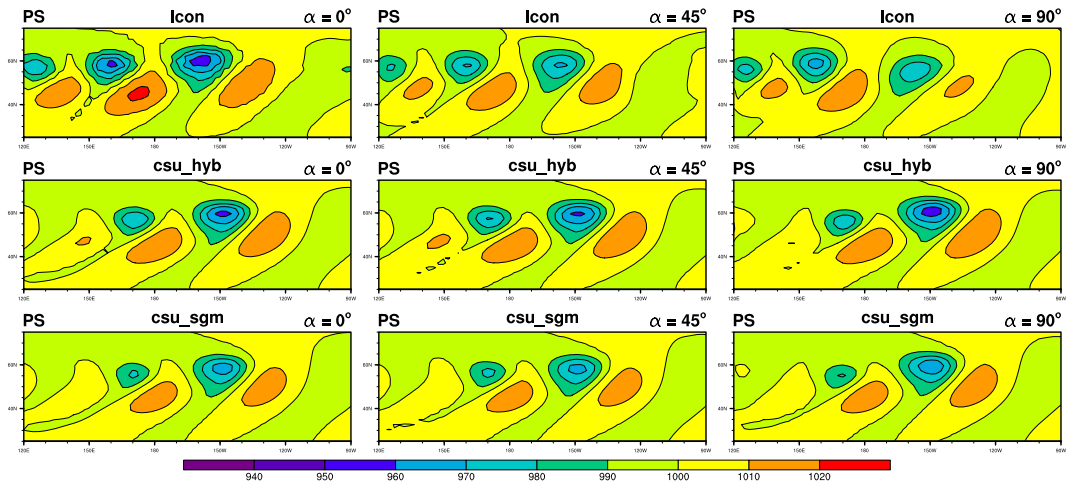
Figure 14: Same as Fig. 13 but for the icosahedral grid models.

Day 9, approximately 1° horizontal resolution at equator
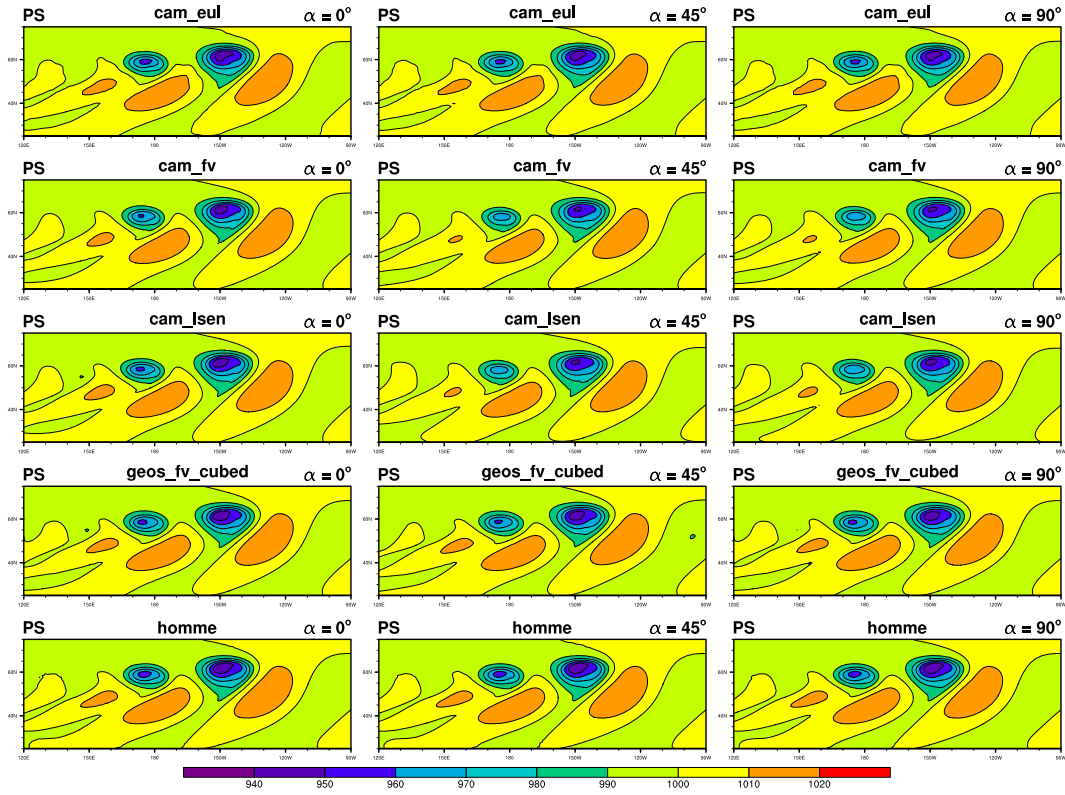
Figure 15: Same as Fig. 13 but for a grid spacing of $\approx 1°$.

Day 9, approximately 1° horizontal resolution at equator
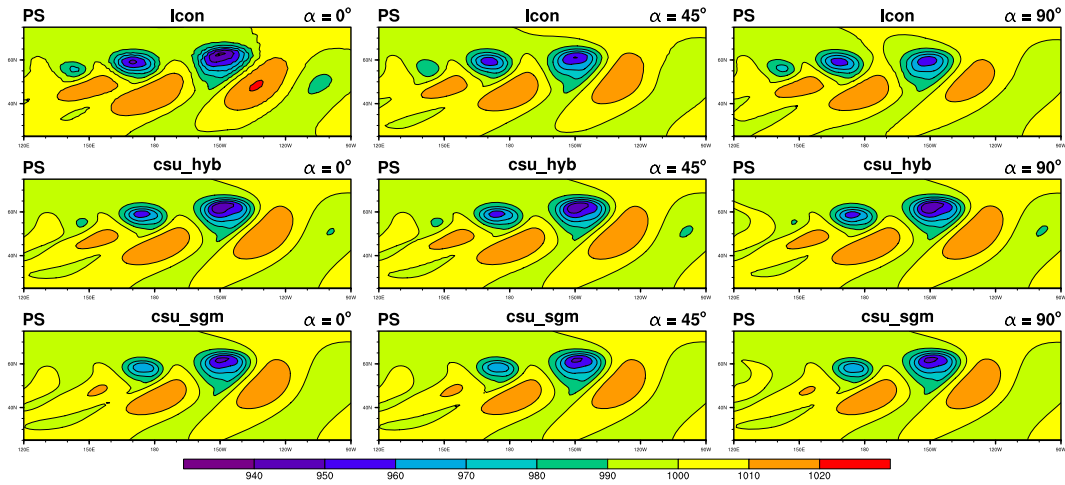
Figure 16: Same as Fig. 15 but for models based on an icosahedral type grid.

Day 9, approximately 2° horizontal resolution at equator
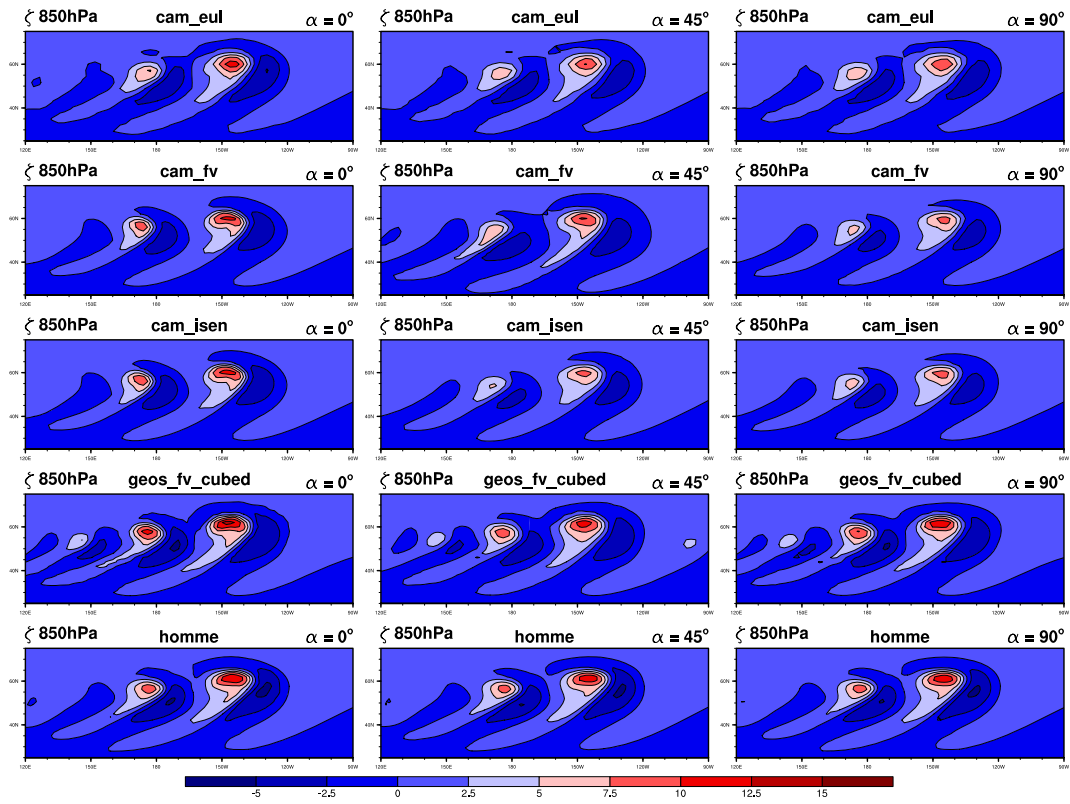
Figure 17: Relative vorticity (day 9) at 850hPa in units of $10^{-5}s^{-1}$ for models based on a regular latitude-longitude and cubed-sphere grids for different rotation angles (left, middle and right columns are $\alpha = 0°$, $45°$ and $90°$, respectively). The models use a grid spacing of $\approx 2°$.

Day 9, approximately 2° horizontal resolution at equator
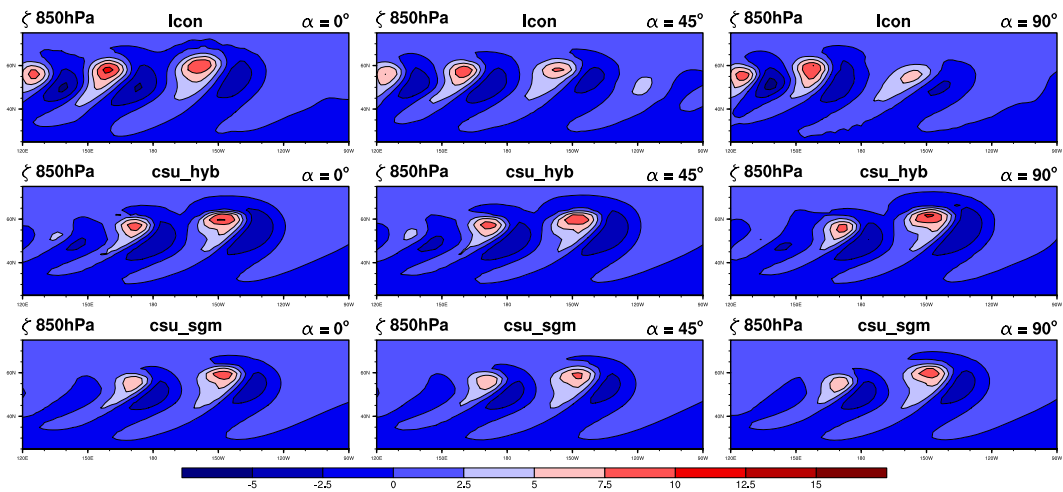
Figure 18: Same as Fig. 17 but for the icosahdral grid models.
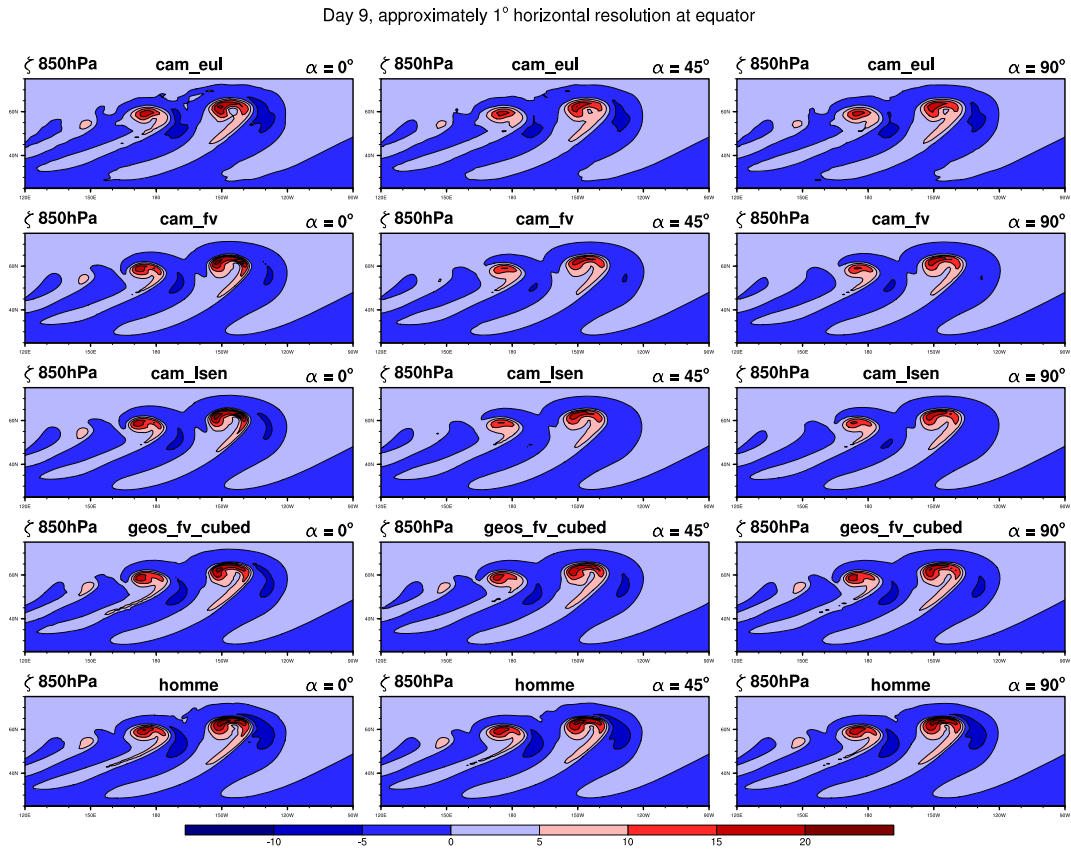
Figure 19: Same as Fig. 17 but for a grid spacing of $\approx 1°$.
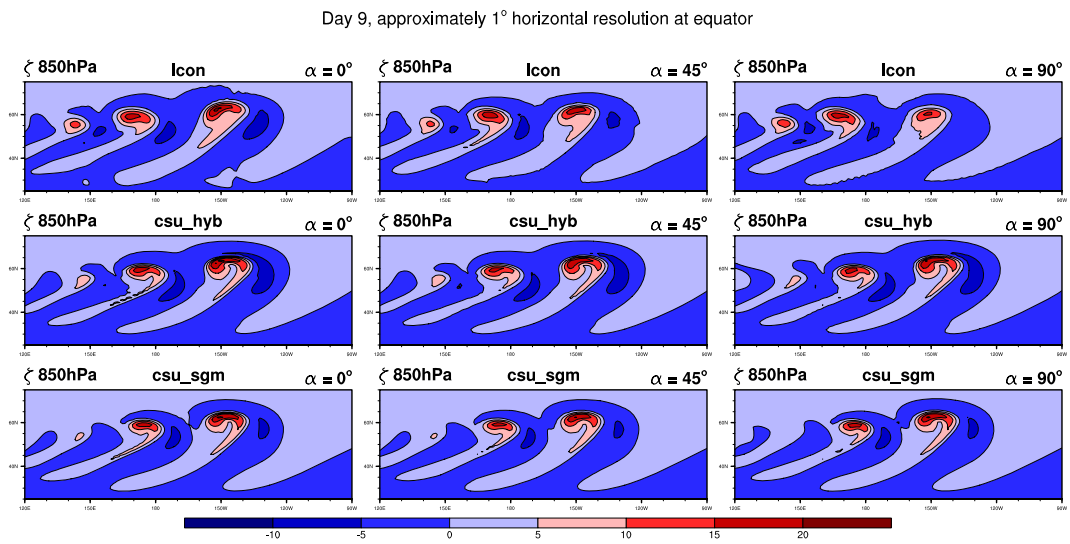
Figure 20: Same as Fig. 19 but for models based on an icosahedral type grid. The unrotated results of the model ICON have been filtered by a standard nine point filter.

Baroclinic wave test, approximately 2° resolution
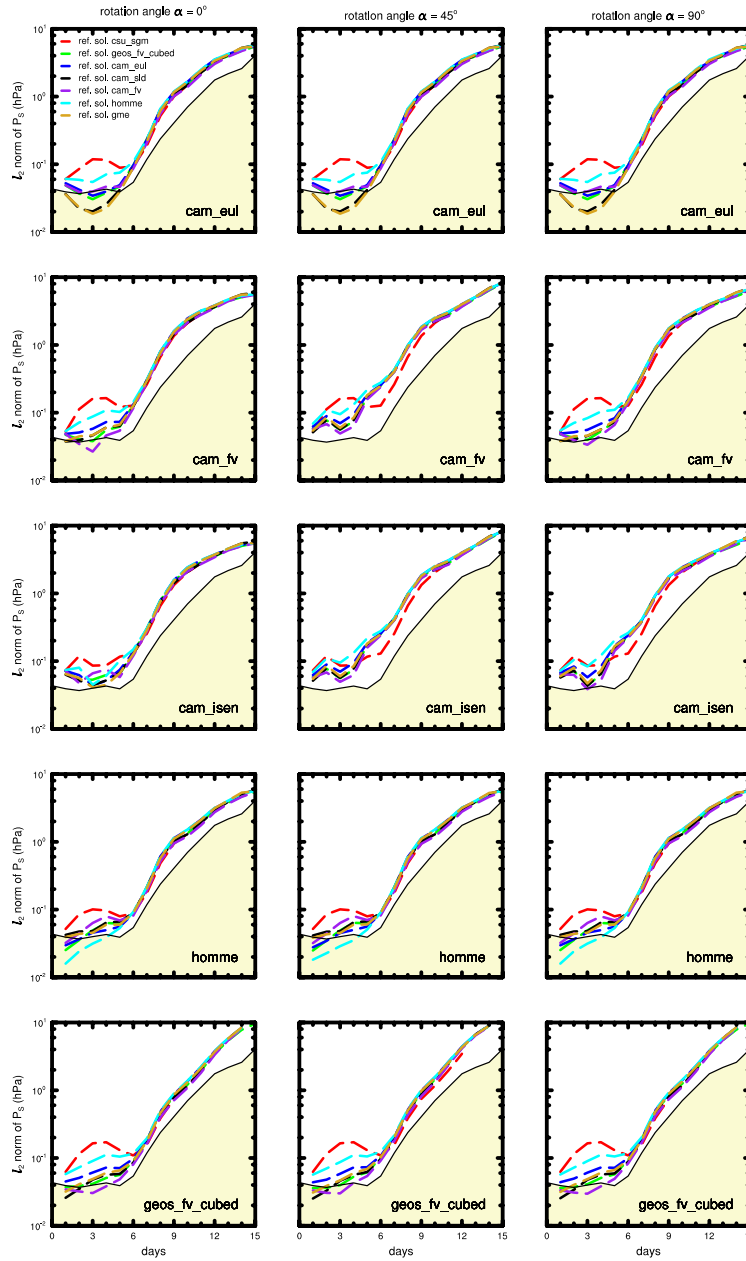
Figure 21: Time series of the root mean square $\ell_2(p_s - p_s^{ref})$ errors (in hPa) using rotation angles (left column) $0°$, $45°$ (middle column) and $90°$ (right column) for CAM_EUL (1st row), CAM_FV (2nd row), CAM_ISEN (3rd row), HOMME (4th row) and GEOS_FV_CUBED (5th row), respectively, at approximately $2°$ horizontal resolution. The errors on each plot have been computed using reference solutions p_s^{ref} from CAM_SLD, GME (see JW06 for description), GEOS_FV_CUBED, CAM_EUL, CAM_FV and CSU_SGM at approximately $0.25°$ resolution, respectively. For the computation of ℓ_2 the reference solutions have been bi-linearly interpolated to the regular latitude-longitude grid on which the model data are available. The yellow region marks the uncertainty of the reference solutions as defined by JW06.
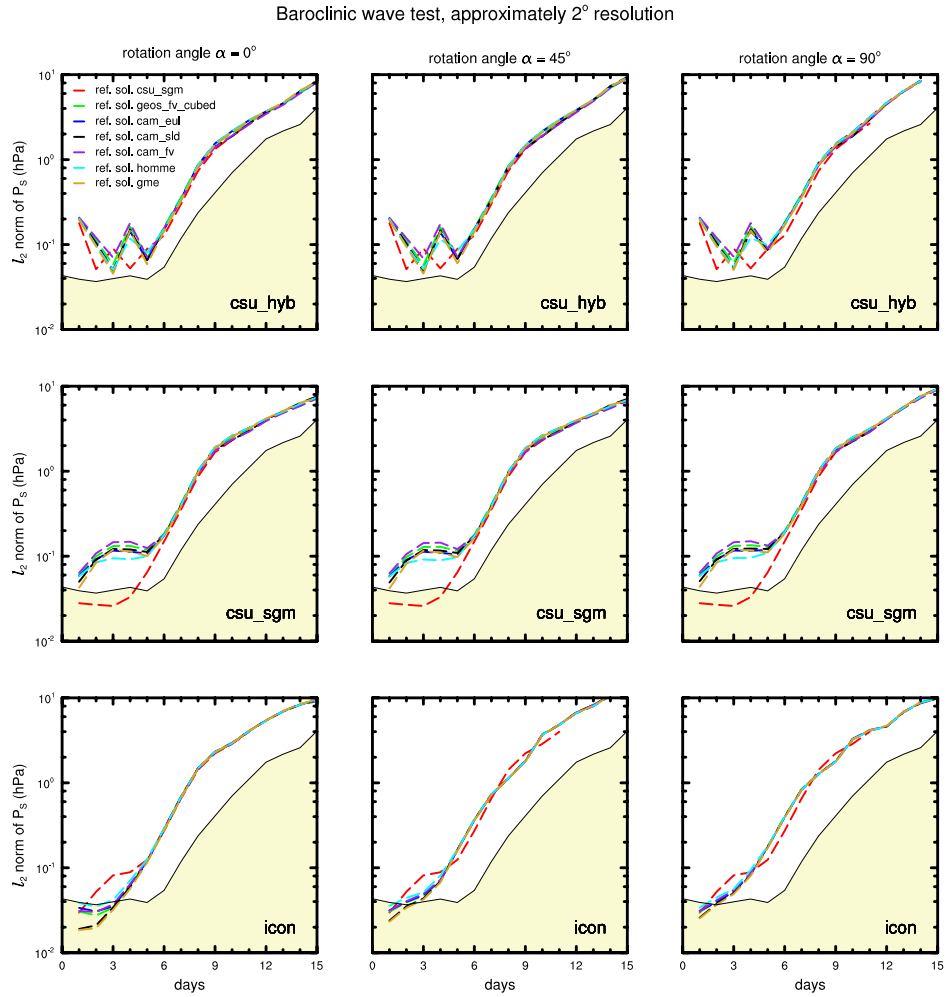
Figure 22: Same as Fig. 21 but for CSU_HYB (1st row), CSU_SGM (2nd row) and ICON (3rd row), respectively.
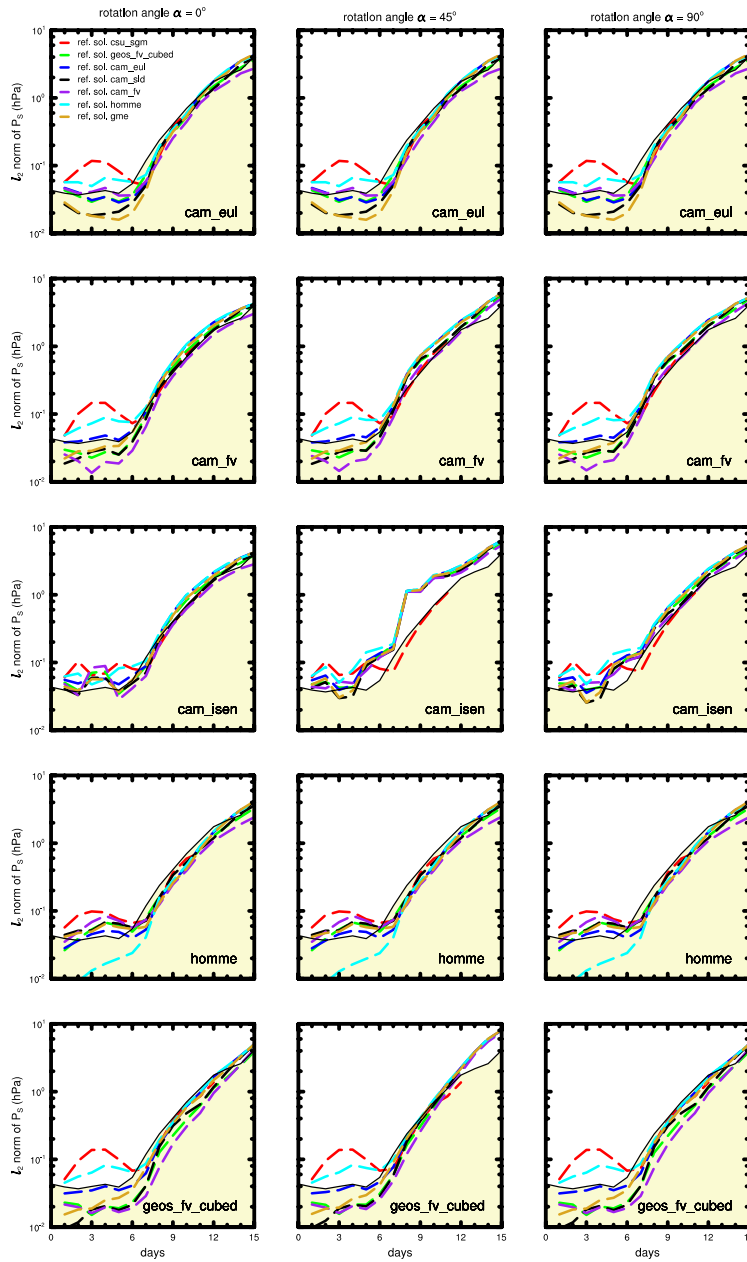
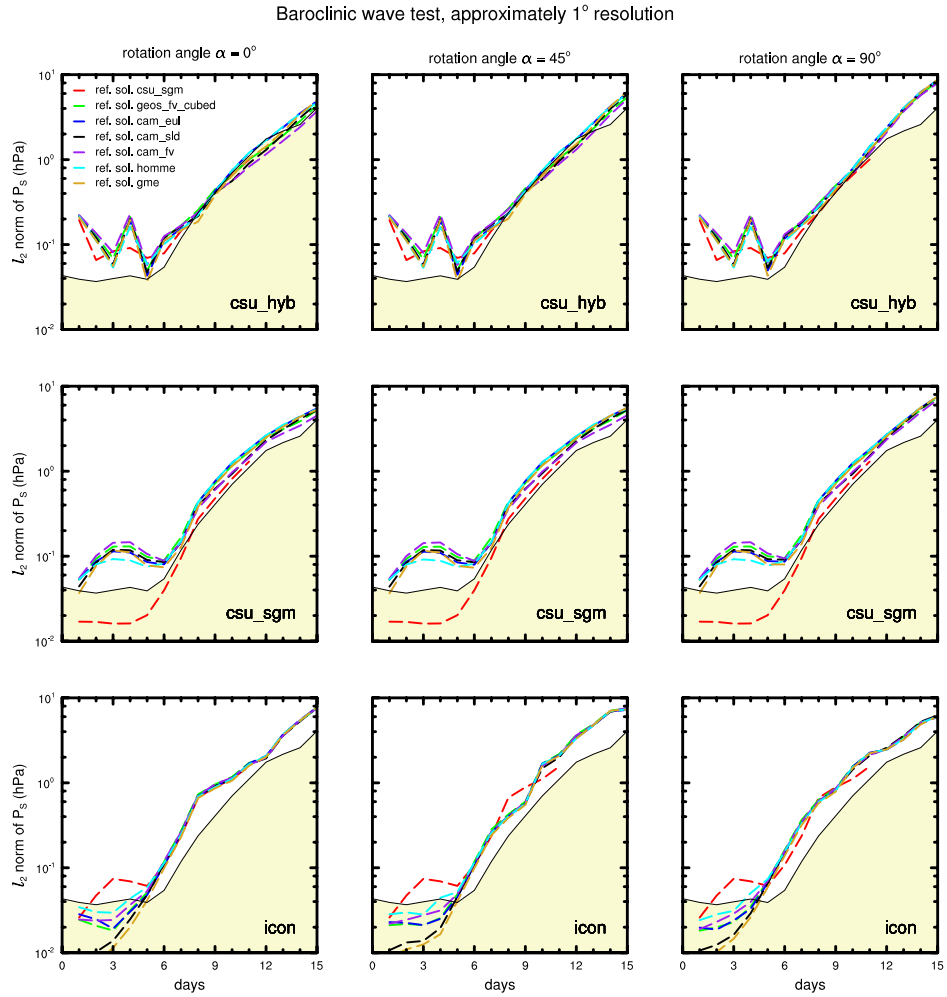Figure 23: Same as Fig. 21 but for approximately 1° horizontal resolution.

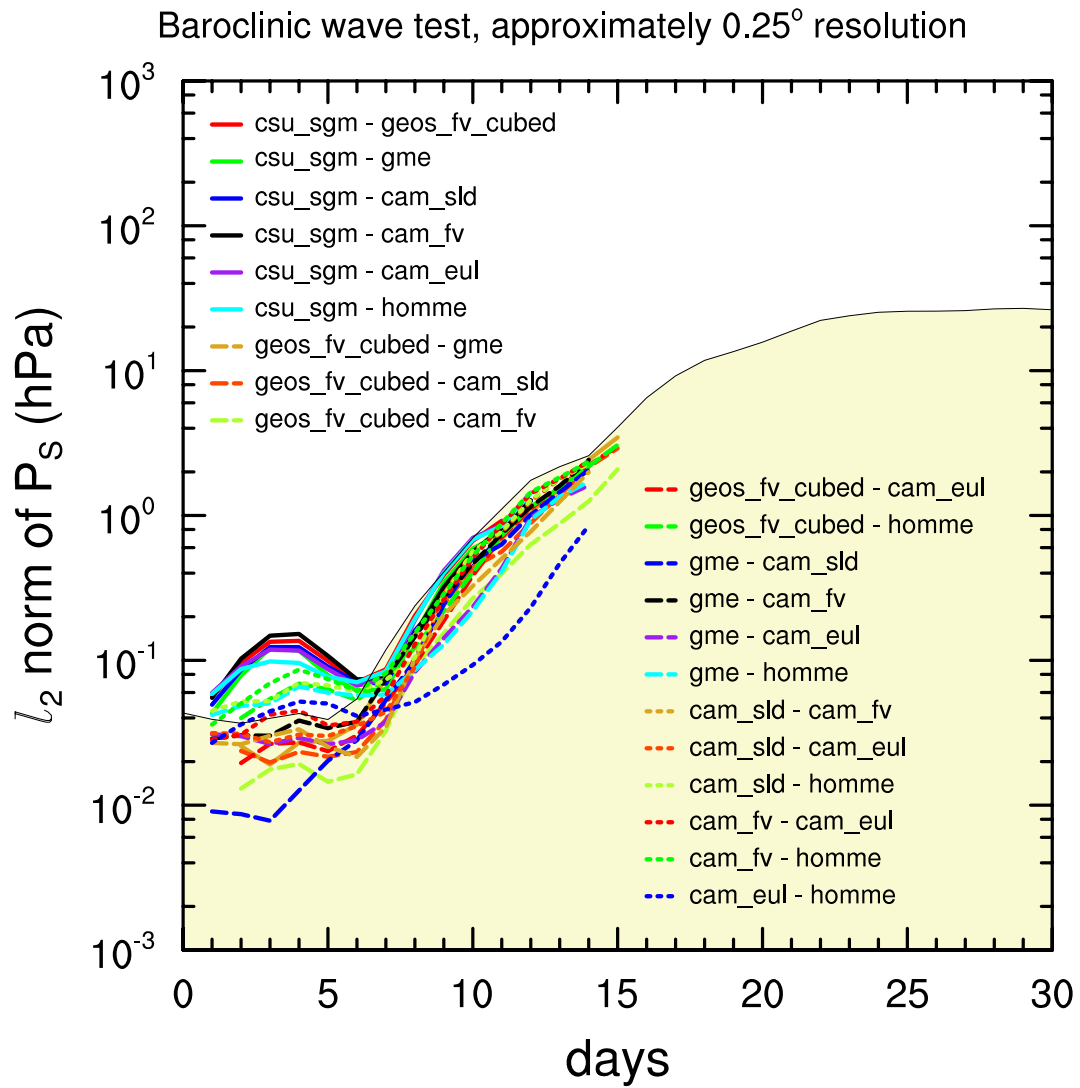Figure 24: Same as Fig. 22 but for approximately 1° horizontal resolution.

Figure 25: Time series of the root mean square ℓ_2 errors (in hPa) between p_s for all high resolution reference solutions ($\approx 1/4°$) used in this paper.